

*The development of a space climatology:
2. the distribution of power input into the
magnetosphere on a 3-hourly timescale*

Article

Accepted Version

Lockwood, M. ORCID: <https://orcid.org/0000-0002-7397-2172>,
Bentley, S. N., Owens, M. J. ORCID: <https://orcid.org/0000-0003-2061-2453>, Barnard, L. A. ORCID:
<https://orcid.org/0000-0001-9876-4612>, Scott, C. J. ORCID:
<https://orcid.org/0000-0001-6411-5649>, Watt, C. E., Allanson,
O. and Freeman, M. P. (2019) The development of a space
climatology: 2. the distribution of power input into the
magnetosphere on a 3-hourly timescale. *Space Weather*, 17
(1). pp. 157-179. ISSN 1542-7390 doi:
<https://doi.org/10.1029/2018SW002016> Available at
<https://centaur.reading.ac.uk/80183/>

It is advisable to refer to the publisher's version if you intend to cite from the work. See [Guidance on citing](#).

To link to this article DOI: <http://dx.doi.org/10.1029/2018SW002016>

Publisher: American Geophysical Union

All outputs in CentAUR are protected by Intellectual Property Rights law, including copyright law. Copyright and IPR is retained by the creators or other copyright holders. Terms and conditions for use of this material are defined in

the [End User Agreement](#).

www.reading.ac.uk/centaur

CentAUR

Central Archive at the University of Reading

Reading's research outputs online

The development of a space climatology: 2. The distribution of power input into the magnetosphere on a 3-hourly timescale

Mike Lockwood¹, Sarah N. Bentley¹, Mathew J. Owens¹, Luke A. Barnard¹, Chris J. Scott¹, Clare E. Watt¹, Oliver Allanson¹ and Mervyn P. Freeman²

¹Department of Meteorology, University of Reading, Earley Gate, P.O. Box 243, Reading, Berkshire, RG6 6BB, UK.

²British Antarctic Survey, High Cross, Madingley Road, Cambridge, CB3 0ET, UK.

Corresponding author: M. Lockwood (m.lockwood@reading.a.uk)

Key Points:

- The normalized distribution of power input to the magnetosphere is set by IMF orientation variability via magnetopause reconnection rate
- 3-hourly normalized power input obeys a Weibull distribution with shape parameter $k=1.0625$ and scale parameter $\lambda=1.0240$ for all years
- Annual means can give the probability of space weather events in the largest 10% and 5% to within one-sigma errors of 10% and 12%, respectively

Abstract

Paper 1 in this series [Lockwood *et al.*, 2018b] showed that the power input into the magnetosphere P_α is an ideal coupling function for predicting geomagnetic “range” indices that are strongly dependent on the substorm current wedge and that the optimum coupling exponent α is 0.44 for all averaging timescales, τ , between 1 minute and 1 year. The present paper explores the implications of these results. It is shown that the form of the distribution of P_α at all averaging timescales τ is set by the IMF orientation factor via the nature of solar wind-magnetosphere coupling (due to magnetic reconnection in the dayside magnetopause) and that at

26 $\tau = 3$ hrs (the timescale of geomagnetic range indices) the normalized P_α (divided by its annual
 27 mean, i.e. $\langle P_\alpha \rangle_{\tau=3\text{hr}} / \langle P_\alpha \rangle_{\tau=1\text{yr}}$) follows a Weibull distribution with k of 1.0625 and λ of 1.0240.
 28 This applies to all years to a useful degree of accuracy. It is shown that exploiting the constancy
 29 of this distribution and using annual means to predict the full distribution gives the probability of
 30 space weather events in the largest 10% and 5% to within uncertainties of magnitude 10% and
 31 12%, respectively, at the one-sigma level.

32 **1. Introduction**

33 In Paper I [*Lockwood et al.*, 2018b] in this series, it was established that the power input into the
 34 magnetosphere, P_α , computed from near-Earth interplanetary data using the physics-based
 35 formulation of *Vasyliunas et al.* [1982], is highly correlated with both the *am* geomagnetic index
 36 over a range of averaging timescales τ between a 3-hours and one year, with an optimum
 37 coupling function of $\alpha = 0.44$. In addition, the SME auroral index was used to show that this
 38 also applies down to $\tau = 1$ min. (Note that allowance for response lag is required at these higher
 39 time resolutions to account for the effect of energy storage in the geomagnetic tail and its
 40 subsequent release during the substorm cycle). The averaging timescale employed is an
 41 important, but often overlooked, consideration in solar wind-magnetosphere coupling studies yet
 42 its effects on behaviour and conclusions can be considerable [*Finch and Lockwood*, 2007;
 43 *Badruddin and Aslam*, 2013]. In the current paper, we study the distribution of 3-hourly P_α
 44 values ($\tau = 3$ hrs.) and investigate why it has the form that it does. The reasons for studying this
 45 distribution are associated with reconstructions of past space weather conditions (see sections 1.1
 46 – 1.3 below), which exploit an important empirical result – namely that the annual distributions
 47 of values of various space weather parameters, X , averaged over an interval τ and divided by
 48 their annual mean, $\langle X \rangle_\tau / \langle X \rangle_{\tau=1\text{yr}}$, are surprisingly constant over time [*Lockwood et al.*, 2017,
 49 2018a]. This is an extremely valuable result, but one which would have greater predictive power
 50 (and in which we could have greater confidence) if we understood why it applies and what its
 51 limitations are. In Paper 3 of this series [*Lockwood et al.*, 2018c], we study the evolution of the
 52 distribution of P_α with τ from the 3 hrs. studied here up to $\tau = 1$ year. Together, these papers
 53 supply much of the understanding of the empirical result that we are searching for.

54 **1.1 Space Climate: reconstructions of annual means of space weather parameters**

55 Recent years have seen the development of reconstructions of past annual mean conditions in
56 near-Earth space. These have been made from historic solar and geomagnetic observations,
57 interpreted using understanding derived from modern measurements made by spacecraft and
58 solar magnetographs. Initially these reconstructions employed single or multiple regression fits
59 of co-incident data, but they have subsequently grown more complex and now also employ
60 physical understanding and model simulations and have been checked using independent
61 datasets, such as observed abundances of cosmogenic isotopes found in terrestrial reservoirs.
62 The first attempt to reconstruct the interplanetary conditions of the past was made by *Feynman*
63 *and Crooker* [1978] who used the geomagnetic *aa* index, which extends back to 1868. This
64 index is based on the range of variation in the horizontal component of the geomagnetic field in
65 3-hour windows (as introduced by *Bartels* [1939]) and has, like all such “range” indices, an
66 approximately square-law dependence on the speed of the solar wind impinging on Earth, V_{sw}
67 [see *Lockwood*, 2013]. However, on annual timescales, *aa* also depends on the near-Earth IMF
68 field strength, B , changes in which therefore also contribute to its long-term drift. *Feynman and*
69 *Crooker* considered various combination scenarios of B and V_{sw} , including assuming that B was
70 constant, in order to derive a long-term variation in V_{sw} . The first separation of these two factors
71 was made by *Lockwood et al.* [1999] who used the relationship between the 27-day recurrence of
72 *aa* and the annual mean V_{sw} to remove the dependence on V_{sw} . Rather than computing the near-
73 Earth IMF B , *Lockwood et al.* evaluated the open solar flux (OSF, a global parameter, being the
74 total magnetic flux leaving the top of the solar corona, whereas B is a local parameter as it only
75 applies to the near-Earth heliosphere). In order to achieve this, these authors used the Ulysses
76 result that the radial component of the heliospheric field is largely independent of heliographic
77 latitude [*Smith and Balogh*, 1995; *Lockwood et al.*, 2004; *Owens et al.*, 2008]. *Solanki et al.*
78 [2000] reproduced the OSF variation deduced by *Lockwood et al.* using the global OSF
79 continuity equation, with sunspot number quantifying the global OSF production rate and with a
80 constant fractional loss rate. This model has subsequently been developed, refined, and used
81 many times [*Solanki et al.*, 2002; *Schrijver et al.*, 2002; *Lean et al.*, 2002; *Wang and Sheeley*,
82 2002; *Mackay et al.*, 2002; *Mackay and Lockwood*, 2002; *Usoskin et al.*, 2002; *Lockwood*,
83 2003; *Wang et al.*, 2002; 2005; *Vieira and Solanki*, 2010, *Steinhilber et al.*, 2010; *Demetrescu et*

84 *al.*, 2010; *Owens et al.*, 2011; *Owens and Lockwood*, 2012; *Goezler et al.*, 2013; *Lockwood and*
85 *Owens*, 2014a;b ; *Wang and Sheeley*, 2013; *Karoff et al.*, 2015; *Rahmanifard et al.*, 2017;
86 *Asvestari et al.*, 2017]. The continuity model allows us to reconstruct the annual mean OSF
87 variation using sunspot number as a proxy for the OSF emergence rate. Hence the OSF variation
88 depends on the integral of the sunspot number and will only be influenced by relatively long-
89 lived differences between the sunspot series employed. Over the interval for which we have
90 reliable and homogeneous geomagnetic data (c. 1845 - present), almost identical results are
91 obtained using the various sunspot number composites available, and all give good matches to
92 the geomagnetic OSF reconstruction [*Lockwood et al.*, 2016a; *Owens et al.*, 2016a]. However,
93 before 1845 the divergence of the various sunspot number reconstruction is greater and this does
94 introduce changes to the derived OSF variation, particularly between the Maunder and Dalton
95 minima (i.e. between about 1710 and 1790) [*Lockwood et al.*, 2016a; *Owens et al.*, 2016b].

96 The continuity model applies to OSF but has also been used to derive reconstructions of the near-
97 Earth IMF, B [e.g. *Rahmanifard et al.*, 2017], which requires understanding of how OSF and B
98 are related. It is often assumed, either explicitly or implicitly, that the two are linearly related
99 [e.g., *Svalgaard and Cliver*, 2010]. In fact, proportionality is a much better assumption than
100 linearity as it avoids the nonsensical possibility of a non-zero, near-Earth IMF B when its source,
101 the OSF, is zero: assuming linearity yields a false “floor” minimum value to B (the intercept
102 value). An assumption of proportionality was made in the analytic equations used in the first
103 reconstruction of OSF by *Lockwood et al.* [1999] – however, this could be done only because the
104 difference between the real OSF- B relation and the assumed proportional one was accounted for
105 in the regressions that were then used to derive OSF from the data [*Lockwood and Owens*, 2011].
106 In general, there are two competing effects that make the OSF- B relationship more complex than
107 either proportional or linear: for a given OSF, the near-Earth heliospheric magnetic field
108 (hereafter called the interplanetary magnetic field, IMF) will decrease with increasing V_{sw}
109 because of the unwinding of the Parker spiral. Secondly, as the mean V_{sw} increases its
110 longitudinal structure also increases which enhances kinematic “folding” of open field lines,
111 increasing B for a given OSF [*Lockwood et al.*, 2009a; b; *Lockwood and Owens*, 2009; *Owens et*
112 *al.*, 2017]. The resulting relationship of OSF and B has been studied by *Lockwood and Owens*
113 [2011] and *Lockwood et al.* [2014a] and allows us to employ the continuity model, which can

114 only apply to a global parameter such as OSF and not to a local one such as B , to model past
115 variations of the near-Earth IMF B from sunspot numbers.

116 *Svalgaard and Cliver* [2005] developed their IDV geomagnetic index from Bartels' u-index
117 [*Bartels*, 1932] and noted that it depended on B , with very little influence of V_{sw} . Indeed,
118 several indices constructed from hourly mean geomagnetic data have this property, whereas
119 range indices depend on both B and V_{sw} [*Lockwood*, 2013]. This is a very important result as it
120 means that combinations of different indices can be used to derive both B and V_{sw} . The long-
121 term variation of B that was derived by *Svalgaard and Cliver* [2005] was questioned by
122 *Lockwood et al.* [2006] because their analysis employed non-robust regression procedures and
123 also because it filled large data gaps in the observed IMF and solar wind speed time-series with
124 interpolated values. (As demonstrated in Paper 1 [*Lockwood et al.*, 2018b], a much more reliable
125 option is to mask out the geomagnetic data during data gaps when the interplanetary data are
126 missing [*Finch and Lockwood*, 2007]). However, the insight provided by *Svalgaard and Cliver*
127 is extremely valuable: *Rouillard et al.* [2007] used it in their reconstruction of both B and V_{sw} ,
128 and *Lockwood* [2014a] used 4 different pairings of different indices to derive both (as well as the
129 OSF), with a full Monte-Carlo uncertainty analysis, back to 1845. Once the distinction between
130 OSF and near-Earth IMF B is allowed for, there is a growing convergence between the different
131 geomagnetic reconstructions of heliospheric parameters [*Lockwood and Owens*, 2011], and also
132 with those from cosmogenic isotopes [*Asvestari and Usoskin*, 2016; *Asvestari et al.*, 2017;
133 *Owens et al.*, 2016b].

134 *Svalgaard and Cliver* [2010] extended the geomagnetic reconstructions back to 1835 using
135 Bartels' work on diurnal variations. However, this results in a data series that is not
136 homogeneous and *Lockwood et al.* [2014a] argue that geomagnetic reconstructions are only
137 reliable for 1845 onwards. What is certain is that the start date cannot be before 1832, when
138 Gauss introduced the first properly-calibrated magnetometer. To extend the series before the start
139 of reliable geomagnetic data we have to employ the models based on sunspot number and the
140 OSF continuity equation. These models can be run from the start of regular telescopic sunspot
141 observations in 1612. *Lockwood and Owens* [2014a] extended the OSF modelling to compute the
142 OSF in the both the streamer belt and in coronal holes and so computed the streamer belt width.

143 The results match well the streamer belt width derived from historic eclipse images [*Owens et*
144 *al.*, 2017]. From this, and from modern magnetograph observations of the streamer belt width,
145 *Lockwood and Owens* [2014b] made deductions about the annual solar wind speeds during the
146 Maunder minimum. The reconstructed streamer belt width and OSF were used by *Owens et al.*
147 [2017], in conjunction with 30 years' output from a data-constrained magnetohydrodynamic
148 model of the solar corona based on magnetograph data, to reconstruct V_{SW} , B and solar wind
149 number density, N_{SW} from sunspot observations. From these reconstructions, annual means of
150 power input into the magnetosphere, P_{α} , have been computed by *Lockwood et al.* [2017].

151 **1.2 The use of annual means in space climate reconstructions**

152 There are a number of reasons why all of the reconstructions discussed in section 1.1 have been
153 restricted to annual means. The first, but least compelling, reason is that the correlations
154 exploited to make the reconstructions are higher for annual means than for data of higher time
155 resolution. This is, at least in part, caused by the cancellation of observation noise in the annual
156 means but there are also some systematic variations that are averaged out. For example, there is a
157 seasonal variation in the ionospheric conductivities influencing any one geomagnetic observatory
158 [*Wallis and Budzinski*, 1981; *Nagatsuma*, 2006; *Finch*, 2008; *Koyama et al.*, 2014]. In the *aa*
159 index, this effect is reduced by averaging data from two sites, one in each hemisphere, but better
160 cancellation of seasonal effects is achieved by the *ap* index with its greater number of stations
161 and the use of conversion tables that allow for season. However, there is still a remnant annual
162 variation in *ap* because the sites are not distributed uniformly or equally in the two hemispheres
163 [*Finch*, 2008] and the *am* index provides a much flatter time-of-day and time-of-year response
164 pattern because of its more even geographical distribution of stations. Other systematic annual
165 variations are introduced by the effects of Earth's dipole tilt and the variation of the Earth's
166 heliographic latitude over the year (see *Lockwood et al.* [2016b], and references therein).

167 However, the fundamental limit that prevents the P_{α} reconstructions being of higher time
168 resolution than annual is the importance of orientation of the near-Earth IMF in driving
169 geomagnetic activity. This issue has been discussed by *Lockwood* [2013] and *Lockwood et al.*
170 [2017b]. It is well known that on short timescales, because of the dominant role of magnetic

171 reconnection, the coupled magnetosphere-ionosphere-thermosphere responds to the polarity and
172 magnitude of the southward component of the IMF (in a suitable frame oriented with respect to
173 the geomagnetic field axis, such as Geocentric Solar Magnetospheric, GSM). As discussed in
174 Paper 1 [Lockwood *et al.*, 2018b], there are two time constants of response. The first is the
175 directly-driven system which responds on a timescale of order a few minutes. The other response
176 is the storage-unloading system, whereby the directly-driven flows store magnetic flux and
177 energy in the magnetospheric tail which is released and deposited in the nightside auroral
178 ionosphere and thermosphere via the substorm current wedge. This generates a second response
179 after a delay of between about 30 and 60 min. The polarity of the southward field component
180 rarely remains constant for more than about 1 hour [Hapgood *et al.*, 1981] and is always
181 fluctuating under the influence of transient events such as coronal mass ejections, co-rotating
182 interaction regions, smaller-scale stream-stream interactions, and turbulence (see review by
183 Lockwood *et al.* [2016b] and references therein). There is very little historical evidence available
184 that could be exploited further to improve reconstructions of timescales shorter than annual
185 means. Matthes *et al.* [2017] have used the (extended) *aa* index to improve time resolution back
186 to 1845 (with consideration of the known limitations of *aa*) and provide a set of plausible
187 scenarios for the Dalton and Maunder minima which occurred before this date. Another
188 potential source of daily information is auroral observations [Legrand and Simon, 1987;
189 Silverman, 1992; Kataoka *et al.*, 2017]. However, there are severe complications introduced by:
190 (1) the great differences between observing sites in the annual variations in hours of darkness and
191 its effect on observation probability; (2) the effect of both secular drift in the Earth's field and of
192 human migration on the numbers of people available to record sightings at latitudes where
193 aurorae occur most frequently; (3) secular change in cloud cover at a given site; (4) the social
194 factors that make recording of sightings fashionable and accurate; (5) subsequent loss of data
195 through catastrophic events such as fires and wars; and (6) the increased use of street lighting in
196 centers of population [Lockwood and Barnard, 2015]. Alternatively, and only after a great deal
197 of further research, it may become possible to also use modelling of the solar corona, and its
198 extension into the heliosphere, based on daily sunspot numbers; however, such applications
199 remain in the future.

200 None of these possibilities are viable at the present time and so there is no source of historic
201 information on IMF orientation at sub-annual times that can be applied back to the Maunder
202 minimum. Hence the interplanetary time series, and their terrestrial space weather responses,
203 cannot be reconstructed. The only solution is to average out the fluctuations in IMF orientation,
204 such that only a dependence on the IMF magnitude, B , remains [Lockwood, 2013]. Averaging
205 over sufficiently long intervals reduces the IMF orientation factor to an approximately constant
206 factor. Lockwood *et al.* [2017] show that employing a single, overall average value for an IMF
207 orientation factor in GSM causes only a 4% error in annual means (as opposed to 10% error for
208 27-day means and a 42% error for 1-day means).

209 **1.3 Space Climatology: reconstructions of distributions of space weather parameters**

210 From the discussion in Section 1.2, it is apparent that we cannot, for the time being at least,
211 construct a time series of data at sub-annual resolution to study the space weather conditions far
212 enough into the past to cover grand minimum conditions. However, this does not mean that we
213 cannot construct a space weather climatology, giving the probability of events exceeding a
214 certain size, by reconstructing the Probability Distribution Functions (PDFs) of space weather
215 parameters. In this area, a surprising and powerful new empirical result has recently emerged:
216 the annual distributions of many space weather indices for a given averaging timescale, τ , as a
217 ratio of its annual mean, (i.e., the PDFs of $\langle X \rangle_{\tau} / \langle X \rangle_{1\text{yr}}$ for a generic space weather index X) are
218 remarkably constant for a given τ . The distributions are quite close to lognormal at all τ but the
219 variance decreases with increasing τ (i.e. the distribution becomes more Gaussian-like).
220 Lockwood *et al.* [2017] showed this result held for daily means ($\tau = 1$ day) during the space age
221 of the power input into the magnetosphere, P_{α} , and of the ap geomagnetic index. This is despite
222 the fact that the relative contributions to geomagnetic activity of recurrent disturbances such as
223 Corotating Interaction Regions (CIRs) and random events (such as impacts by Coronal Mass
224 Ejections) varied considerably during this interval [Holappa *et al.*, 2014]. Lockwood *et al.*
225 [2018a] have shown that this result also holds for all of the full ap index data sequence (i.e., for
226 1932-2016) and all years of the aa index data (for 1868-2016).

227 Figure 1 stresses how ubiquitous this result is for space weather indices. Because the
 228 distributions maintain an almost constant shape, the number of events in each year above a given
 229 fixed threshold show a monotonic variation with the average value for that year [see *Lockwood et*
 230 *al.*, 2017]. Figure 1 is for an example τ of 1 day, showing scatter plots of $f[X > X_0]$, the fraction
 231 of days for a given year in which the daily mean of a parameter X exceeds its 95 percentile ($X >$
 232 X_0 , where X_0 is computed from the whole dataset), as a function of the annual mean of that
 233 parameter $\langle X \rangle$. Figure 1(a) is for the *ap* index using all the available data (for 1932-2016); 1(b)
 234 is for the *Dst* index (1957-2016); (c) the *AE* index (1968-2016); (d) the *AU* index (1968-2016);
 235 (e) the *AL* index (1968-2016); and (f) the power input into the magnetosphere, P_α , computed
 236 from interplanetary data for a coupling exponent $\alpha = 0.44$ (1996-2016, although some years are
 237 not used as data gaps are too numerous and too long, see Paper 1 and *Lockwood et al.* [2017]). In
 238 each case, an increase in the average disturbance level (which means increasingly negative in the
 239 cases of *AL* and *Dst*) is associated with an increase in the fraction of days with disturbance in the
 240 top 5% of the overall distribution for that parameter. The scatter is greatest for *Dst*, but very
 241 small for *AL*, but this finding is of value to the climatology of a wide range of terrestrial space
 242 weather disturbance indices. The mauve lines in each panel of Figure 1 are third-order
 243 polynomial fits to these data points, constrained to pass through the origin (so that $f_{\text{fit}}[X > X_0] = 0$
 244 when $\langle X \rangle_{\tau=1\text{yr}} = 0$). The Table in Part 5 of the Supporting Information gives the coefficients for
 245 these fits for each index and also the values of Δ_{rms} , the root-mean-square (r.m.s.) of the
 246 fractional fit residuals. These confirm that the *AL* index has the lowest scatter. In fact the rank
 247 order by Δ_{rms} is very revealing and shows a dependence on the latitudinal difference of the
 248 observing stations from the auroral oval. If we consider that the origin of this behaviour is the
 249 power input into the magnetosphere, the close adherence to the relationship by *AL* is consistent
 250 with this index being a good indicator of power released from the geomagnetic tail lobes as part
 251 of the storage/release behavior. If this is indeed the case, the fact that *AU* agrees slightly less
 252 well indicates that the power input to the magnetosphere is a slightly less good predictor of the
 253 directly-driven current system. The *AE* index is midway between *AL* and *AU* in its behaviour,
 254 being the difference of the two ($AE = AU - AL$ where *AL* is negative). The next closest agreement
 255 is the *Ap* index, which is a planetary index recorded at middle latitudes that is very sensitive to
 256 the substorm current wedge and so well correlated with *AL* (see Supporting Information file
 257 attached to Paper 1). The agreement for the *Dst* index is still good but not as good for the other

258 geomagnetic indices. Ideally, if the relationships shown in Figure 1 all arose from the power
259 input to the magnetosphere, then the relationship for P_α/P_0 would be stronger than for all the
260 geomagnetic indices. However, the scatter is greater for P_α/P_0 than for any of the geomagnetic
261 indices except *Dst*. We have repeated the analysis for G_α/G_0 where $G_\alpha = P_\alpha/\sin^4(\theta/2)$, and hence
262 is the power input without the IMF orientation factor, and G_0 is the overall average of G_α . Note
263 that whereas the geomagnetic indices have availability of essentially 100%, that of G_α is 96%
264 and that of P_α is 86% for daily means (because, as described in Paper 1, we require just 9
265 samples in an hour to give an error below 5% for all the parameters used to compute G_α , whereas
266 for the IMF orientation factor the same error requires 50 samples in an hour). Interestingly, Δ_{rms}
267 is considerably smaller for G_α/G_0 than for P_α/P_0 and so much of the scatter for P_α/P_0 is
268 introduced by the IMF orientation factor. This may be associated with the limitations of the
269 IMF orientation factor used, but it seems likely that data gaps also contributed to the
270 additional scatter for P_α/P_0 . What does seem to be clear is that the scatter gets increasingly
271 larger for geomagnetic indices which are influenced by currents other than the nightside auroral
272 electrojet because they employ stations that are further away from it.

273 We stress here that although the bulk (or “core”) of the PDFs are usually best fitted by something
274 like a lognormal distribution [e.g., *Riley and Love, 2017*], the extreme tail of the distribution is
275 not generally well described by the core distribution and so the result will not, in general, hold
276 for the number of the most extreme events [*Redner, 1990*]. In studies of extreme events using
277 “Extreme Value Statistics” (EVS), a lognormal distribution has often been combined with a
278 differently-shaped tail [e.g. *Vörös et al., 2015; Riley and Love, 2017*]. Hence, although the use
279 of this result can tell us about the occurrence of “large” events (in the top 5%), we should not
280 expect it to hold well for the most extreme events. The relationship of large storms in the tail of
281 the core distribution to extreme-event “superstorms” is discussed further in Paper 3 [*Lockwood et*
282 *al., 2018c*].

283 In the present paper, we exploit a number of findings that were presented in Paper 1 [*Lockwood*
284 *et al., 2018a*], namely: (1) that statistical studies of solar wind -magnetosphere coupling and
285 coupling functions that employ data from before 1995 are unreliable and likely to be seriously in
286 error because of the presence of more and longer gaps in the interplanetary data series; (2) the

287 coupling exponent determining the power input to the magnetosphere, α , shows no significant
 288 variations with averaging timescale, τ , and the optimum value is $\alpha = 0.44$ at all τ studied (which
 289 was varied between 1 minute and 1 year); (3). annual values of power input to the magnetosphere
 290 P_α derived from combining annual means of the component interplanetary factors (the “average-
 291 then-combine” method) are not exactly the same as annual means of P_α that are computed at high
 292 time resolution and then averaged (the “combine-then-average” method); however, they are a
 293 usable approximation to within an error of about 5%; and (4) the uncertainty in the α estimate
 294 influences the magnitude of the average power into the magnetosphere, P_o , but has negligible
 295 effect on the waveform of the variation in P_α and hence on the ratios $P_\alpha / \langle P_\alpha \rangle_{\tau=1\text{yr}}$. The last point,
 296 (4), comes from further consideration of Figure 7 of Paper 1. Part (b) of that figure shows that
 297 the estimate of the average power into the magnetosphere, P_o , rises hyperbolically with α such
 298 that the maximum range of fitted α (0.40-0.48) causes a variation in P_o between $0.3 \times 10^{19}\text{W}$ and
 299 $0.6 \times 10^{19}\text{W}$. However, part (d) of that figure shows the distributions of P_α / P_o are very similar for
 300 this range of α , all being lognormal in form. This is quantified in part (c) of the figure which
 301 plots the ratios of P_α / P_o to the values for the optimum $\alpha = 0.44$. This weak dependence of P_α / P_o
 302 on the precise values of α around the optimum value is also reflected in the flat-topped nature of
 303 the correlograms shown in Figures 4a and 5a of Paper 1. Thus, although the estimate of the
 304 absolute level of power input to the magnetosphere (averaging P_o for all data and $\langle P_\alpha \rangle_{\tau=1\text{yr}}$ for
 305 annual means) depends strongly on the value of α , the waveform of the variation in P_α (that is
 306 tested by correlation studies) is only weakly dependent on α in the uncertainty range around the
 307 optimum value.

308 **2. Analysis of the contributions to the magnetospheric Power input**

309 The derivation of the equation for the power input to the magnetosphere (given in Paper 1), is
 310 reprised in the Supporting Information file attached to this paper for completeness. This file also
 311 includes a review of why the IMF magnitude is used (B) instead of the component transverse to
 312 the sun-Earth line (B_T) and a confirmation that the best IMF orientation factor is $\sin^4(\theta_{\text{GSM}}/2)$,
 313 using 20 years’ data of both 1-minute and 3-hour resolution and with many fewer, and much
 314 shorter, data gaps.

315 The result that the annual distribution of the normalized power input into the magnetosphere
 316 $\langle P_\alpha \rangle_\tau / \langle P_\alpha \rangle_{\tau=1\text{yr}}$ has an approximately constant, quasi-lognormal form is a purely empirical one.
 317 Figure 2 gives an initial indication of why it applies, by looking at the annual distributions of $R =$
 318 $\log_{10}(\langle X \rangle_{\tau=1\text{min}} / \langle X \rangle_{\tau=1\text{yr}})$ where X is one of the parameters of near-Earth space that contributes to
 319 P_α . Equation (6) of Paper 1 (equation (S7) in the Supporting Information) shows that relevant
 320 parameters are: the mean ion mass of the solar wind, m_{sw} ; its number density, N_{sw} ; its speed, V_{sw} ;
 321 the strength of the IMF frozen-in to the solar wind flow, B ; the clock angle that the IMF makes
 322 with the north in the GSM frame of reference, θ_{GSM} (defined by $\theta_{\text{GSM}} = \arctan(|B_{\text{YM}}|/B_{\text{ZM}})$, where
 323 B_{YM} and B_{ZM} are the Y and Z components of the IMF in the GSM frame); Earth's magnetic
 324 moment, M_{E} ; and a constant k_3 . We here group terms according to their exponent in the
 325 expression for P_α . If the ratio $(\langle X \rangle_\tau / \langle X \rangle_{\tau=1\text{yr}})$ is lognormally distributed, R will be normally
 326 distributed about a mode and mean value of zero. Parts (a), (c), (e) and (g) of Figure 2 show the
 327 annual distributions of R for 1996-2017 (inclusive) for 1-minute averages ($\tau = 1\text{min}$) where X is,
 328 respectively: the IMF, B ; the solar wind mass density, $m_{\text{sw}}N_{\text{sw}}$; the solar wind speed, V_{sw} ; and
 329 the IMF orientation factor, $\sin^4(\theta_{\text{GSM}}/2)$. In each case, the vertical axis gives $N/1000$, where N is
 330 the number of 1-minute averaged samples in bins of R that are 0.01 wide. There are 11.13
 331 million 1-minute samples for which all parameters in P_α are available out of a possible total of
 332 12.10 million for this interval, an availability of 92.1%. All the plots show similar distributions
 333 in the different years. Those for B , $m_{\text{sw}}N_{\text{sw}}$, and V_{sw} , in parts (a), (c) and (e) do indeed reveal
 334 near-Gaussian forms (on the logarithmic scale, R). They are not exactly Gaussian: that for V_{sw} is
 335 slightly asymmetric and the peaks for $m_{\text{sw}}N_{\text{sw}}$ tend to be slightly below the ideal value of zero
 336 (however, as noted below, the weighting of the $m_{\text{sw}}N_{\text{sw}}$ factor in P_α is small). The
 337 corresponding right hand plots (b), (d) and (f) show the variations in the variances of these
 338 distributions in R , σ_{R} for each year (normalized to their overall means for all years, i.e. $\sigma_{\text{R}} / \langle \sigma_{\text{R}} \rangle$).
 339 By definition, the mean of each of these variations is unity, shown by the horizontal black line in
 340 each plot, and the surrounding grey areas show plus and minus one standard deviation about this
 341 mean. These show the variance is constant from year to year to within 6.9% (at the 1-sigma
 342 level) for B , 7.9% for $m_{\text{sw}}N_{\text{sw}}$, and 11.2% for V_{sw} .

343 The distribution is quite different for the $\sin^4(\theta_{\text{GSM}}/2)$ factor shown in Figure 2g. The annual
 344 distributions of R in Figure 2g show that $\sin^4(\theta_{\text{GSM}}/2)$ is far from lognormal in form (note the
 345 very large number of samples at $R = -1$, corresponding to $\sin^4(\theta_{\text{GSM}}/2) = 0$: the peak N is always
 346 for the extreme bin plotted at $R = -1$ (which is for $-\infty \leq R < -0.99$). Note that $R = -\infty$ and $R =$
 347 -0.99 correspond to $(\langle X \rangle_{\tau=1\text{min}} / \langle X \rangle_{\tau=1\text{yr}})$ of 0 and 0.1036: given that the average $\sin^4(\theta_{\text{GSM}}/2)$ for
 348 all years is 0.355 to within about 5% [Lockwood *et al.*, 2017], this bin covers a range of
 349 $\sin^4(\theta_{\text{GSM}}/2)$ of just 0 to ≈ 0.036 and yet 21% of 1-minute samples lie in this small range of
 350 $\sin^4(\theta_{\text{GSM}}/2)$ (which is for northward IMF with θ_{GSM} less than about 51.8°). N varies between
 351 57530 and 68225 for this $\sin^4(\theta_{\text{GSM}}/2)$ bin, depending on the year. However, Figure 2h shows
 352 the year-to-year variability is low for $\sin^4(\theta_{\text{GSM}}/2)$, with $\sigma_R / \langle \sigma_R \rangle$ being constant to within 3.2%
 353 at the 1-sigma level. To understand the implications for the $P_\alpha / \langle P_\alpha \rangle_{\tau=1\text{yr}}$ distribution we note
 354 that from the equation for P_α (equation (6) of Paper 1 and (S7) of the Supporting Information):

$$\begin{aligned}
 355 \quad \log_{10}(P_\alpha / \langle P_\alpha \rangle_{\tau=1\text{yr}}) &= \log_{10}(P_\alpha) - \log_{10}(\langle P_\alpha \rangle_{\tau=1\text{yr}}) \\
 356 &= \log_{10}(k_3) + a \log_{10}(B) + b \log_{10}(m_{\text{sw}} N_{\text{sw}}) + c \log_{10}(V_{\text{sw}}) + d \log_{10}(\sin^4(\theta_{\text{GSM}}/2)) - \log_{10}(\langle P_\alpha \rangle_{\tau=1\text{yr}}) \\
 357 & \hspace{15em} (1)
 \end{aligned}$$

358 Where for the best-fit α of 0.44 found in Paper 1

$$359 \quad a = 2\alpha = 0.88 \hspace{15em} (2)$$

$$360 \quad b = (2/3 - \alpha) = 0.227 \hspace{15em} (3)$$

$$361 \quad c = (7/3 - \alpha) = 1.893 \hspace{15em} (4)$$

$$362 \quad \text{and } d = 1 \hspace{15em} (5)$$

363 Figure 9b of paper 1 shows that, to a good approximation (error $\approx \pm 5\%$), annual “average-then-
 364 combine” values of P_α are equal to the “combine-then-average” values, hence

$$365 \quad \langle P_\alpha \rangle_{\tau=1\text{yr}} \approx k_3 (\langle B \rangle_{\tau=1\text{yr}})^{2\alpha} (\langle m_{\text{sw}} N_{\text{sw}} \rangle_{\tau=1\text{yr}})^{(2/3-\alpha)} (\langle V_{\text{sw}} \rangle_{\tau=1\text{yr}})^{(7/3-\alpha)} \langle \sin^4(\theta_{\text{GSM}}/2) \rangle_{\tau=1\text{yr}} \quad (6)$$

366 Substituting for $\log_{10}(\langle P_\alpha \rangle_{\tau=1\text{yr}})$ in (1) using (6) gives

$$367 \quad \log_{10}(P_\alpha / \langle P_\alpha \rangle_{\tau=1\text{yr}}) - a \log_{10}(B / \langle B \rangle_{\tau=1\text{yr}}) + b \log_{10}(m_{\text{sw}} N_{\text{sw}} / \langle m_{\text{sw}} N_{\text{sw}} \rangle_{\tau=1\text{yr}}) + \\ 368 \quad c \log_{10}(V_{\text{sw}} / \langle V_{\text{sw}} \rangle_{\tau=1\text{yr}}) + d \log_{10}(\sin^4(\theta_{\text{GSM}}/2) / \langle \sin^4(\theta_{\text{GSM}}/2) \rangle_{\tau=1\text{yr}}) \quad (7)$$

369 Equation (7) shows that the distribution of $\log_{10}(P_\alpha / \langle P_\alpha \rangle_{\tau=1\text{yr}})$ is the weighted sum of those
 370 shown in Figure 2. The combined contribution of the terms in B , $m_{\text{sw}} N_{\text{sw}}$, and V_{sw} remains close
 371 to Gaussian (on the logarithmic scale of R), dominated by the distribution of V_{sw} . However, the
 372 corresponding distribution for $\sin^4(\theta_{\text{GSM}}/2)$ is very far from Gaussian. From equations (2) - (5)
 373 this last term has a weighting of $d/(a+b+c+d) = 1/4$. Thus the dependence of P_α on $\sin^4(\theta_{\text{GSM}}/2)$
 374 perturbs the distribution of $P_\alpha / \langle P_\alpha \rangle_{\tau=1\text{yr}}$ from the quasi-lognormal form that it would otherwise
 375 have had. However, the right hand panels of Figure 2 explain the small year-to-year variation in
 376 the shape of the distribution of $P_\alpha / \langle P_\alpha \rangle_{\tau=1\text{yr}}$ because each parameter has a quite constant
 377 standard deviation of its R variation, i.e. the standard deviation of X is approximately
 378 proportional to the mean. It should be remembered that Figure 2 is for 1-minute averaged data,
 379 and it becomes important to understand the effect of the averaging timescale, τ . It is not, in itself
 380 of great importance or application in this paper that some of the parameters in P_α are quasi-
 381 lognormally distributed at high time resolution; however, it does make their evolution with τ
 382 more understandable. This is because on averaging over a larger τ , the Gaussian distributions in
 383 the logarithmic R parameter remain Gaussian and become narrower because of the central limit
 384 theorem [Heyde, 2006; Fischer, 2011]. As a result, the distributions of the X parameters remain
 385 lognormal but evolve in shape, becoming less asymmetric. However, shown by Figure 2 of
 386 Lockwood *et al.* [2017], the highly non-Gaussian distribution of $\sin^4(\theta_{\text{GSM}}/2)$, shown here in
 387 figure 2g, varies in a complex way as the averaging timescale, τ , is increased.

388 In order to analyze the behavior of the distribution of power input into the magnetosphere P_α
 389 with averaging timescale τ , we here break equation (6) in Paper 1 [Lockwood *et al.*, 2018b] into
 390 five terms

$$391 \quad P_\alpha = (k_3 M_E^{2/3}) F_B F_V F_N F_\theta \quad (8)$$

$$392 \quad \text{where } F_B = B^{2\alpha}, \quad (9)$$

$$393 \quad F_V = V_{sw}^{(7/3-\alpha)}, \quad (10)$$

$$394 \quad F_N = (m_{sw} N_{sw})^{(2/3-\alpha)}, \quad (11)$$

$$395 \quad \text{and } F_\theta = \sin^4(\theta_{GSM}/2) \quad (12)$$

396 We now analyze the variation of annual means of these terms and their distributions around those
 397 means. In each case, we take the distribution of 3-hourly means ($\tau = 3\text{hr.}$, the resolution of range
 398 geomagnetic indices, which is longer than the average substorm cycle duration so we are
 399 integrating over substorm cycles) as a ratio of the annual mean value. This lets us look at the
 400 contributions of the various terms, not only to the variation in annual means of P_α , but also to the
 401 distributions of $\langle P_\alpha \rangle_{\tau=3\text{hr}} / \langle P_\alpha \rangle_{1\text{yr}}$.

402 **2.1 The effect of the IMF**

403 Figure 3 analyses the behavior of the term in P_α that depends on the IMF magnitude B , F_B
 404 (equation 9). Paper 1 shows that 0.44 ± 0.02 for $\tau = 3\text{hrs}$ gives the optimum agreement with the
 405 *am* index [Lockwood *et al.*, 2018b], the best estimate of F_B reduces to $B^{0.88}$. In Figure 3a, the
 406 annual distributions of 3-hourly values of F_B (normalized for convenience to its overall mean for
 407 1995-2017 [F_B]_o) are shown as vertical slices and as a function of year along the horizontal axis.
 408 We use the criterion for a valid 3-hourly mean established in Paper 1. The number N of the 61126

409 valid 3-hourly means of $F_B/[F_B]_o$ obtained during 1995-2017 (a data availability of 91.0%) is
 410 color-coded in bins of $F_B/[F_B]_o$ that are 0.01 wide. The back line gives the mean values of these
 411 distributions and displays a clear solar cycle variation, with larger values at sunspot maximum
 412 (around 2002 and 2014), as expected. The distribution for all years is shown in Figure 3b by the
 413 gray histogram which shows N/N_{\max} as a function of $F_B/[F_B]_o$, where N_{\max} is the peak value of N .
 414 *Lockwood et al.* [2017; 2018a] have shown that the annual distributions of $\langle P_\alpha \rangle_{\tau=3\text{hr}} / \langle P_\alpha \rangle_{\tau=1\text{yr}}$
 415 are remarkably constant from year to year and Figure 3c investigates the corresponding
 416 contribution of the IMF term by showing the distributions of $F_B / \langle F_B \rangle_{\tau=1\text{yr}}$ (where the means F_B
 417 are also taken over $\tau = 3\text{hrs}$: note that, hereafter, values given without the average symbols and a
 418 τ value subscript are 3 hourly values), in the same format as Figure 3a and the number N is again
 419 counted in bins 0.01 wide. The black line shows the annual means which, by virtue of the
 420 normalization, are always unity. The distributions for the different years are very similar and the
 421 logarithm of their variances ν is close to constant, as shown in Figure 3e. The distribution for all
 422 years is shown by the gray histogram in Figure 3d, where N is again normalized to its peak value.
 423 As expected from Figure 2a, this distribution is well matched by the best-fit (using least squares)
 424 log-normal distribution shown in mauve which has unity mean and a variance ν of 0.120. The
 425 r.m.s. deviation of the fitted lognormal from the observed N/N_{\max} distribution is $\delta_{B,\text{logn}} =$
 426 2.4×10^{-2} : we use this parameter to compare the quality of this fit to others presented in the
 427 subsequent sub-sections. Note that the largest values are not as well fitted, as tends to be the case
 428 for all the fits to the core distribution presented in this paper, indicating the need to use extreme
 429 value statistics to add an appropriate tail to the distribution.

430 Figures 4-7 are equivalent to Figure 3 for the other factors in the equation (8). Note that the y
 431 axis scales are the same for each panel within each figure but are not the same for all figures. We
 432 noted that some of the parameters showed largest deviations in 2003, a solar maximum year in
 433 which the major series of ‘‘Halloween’’ storms occurred during the interval 19th October – 7th
 434 November. The energetic particles associated with these storms themselves caused some data
 435 gaps, but as a test we removed the whole interval and found no detectable differences in Figures
 436 3-7. Hence even the largest storms do not perturb the distributions shown.

437 2.2 The effect of the solar wind speed

438 Figure 4 is the same as Figure 3 but for the term in P_α that depends on the solar wind speed, F_V
 439 (equation 10). As for the IMF term, taking the distribution of 3-hourly values and dividing by
 440 the annual mean gives a near lognormal distribution that is very similar from year to year. The
 441 solar cycle variation in F_V has almost been removed by this normalization; however, there is
 442 some residual effect of the dominance of recurrent fast streams in the declining phase of the solar
 443 cycle when Earth intersects long-lived, fast solar-wind streams [*Cliver et al.*, 1996; *Tsurutani et*
 444 *al.*, 2006] emanating from coronal holes that have expanded to low heliospheric latitudes [*Wang*
 445 *et al.*, 1996] and rotating with the equatorial photosphere approximately every 25 days. They
 446 slightly raise the distribution variances in the declining phases (seen in Figure 4e, and also as the
 447 increased difference between the mode and mean values in Figure 4c, particularly around 2008).

448 The normalized distribution of $F_V/\langle F_V \rangle_{\tau=1\text{yr}}$ for $\tau = 3\text{hrs}$ and all years is shown in Figure 4d by
 449 the grey histogram which has been fitted with log-normal distribution with a mean of unity and
 450 variance $\nu = 0.127$ (mauve line). This is a similar, but slightly higher, variance than for the IMF
 451 factor F_B . The RMS deviation of the fitted lognormal from the observed N/N_{max} distribution is
 452 $\delta_{V,\text{logn}} = 3.6 \times 10^{-2}$ which is a 50% larger than that for F_B .

453 2.3 The effect of the solar wind mass density

454 Figure 5 is the same as Figure 3 but for the term in P_α that depends on the solar wind mass
 455 density, F_N (equation 11). Figure 4a shows that there is a very slight solar cycle variation in the
 456 distributions and mean of F_N , but none for $F_N/\langle F_N \rangle_{\tau=1\text{yr}}$. Note that Figure 5a shows an increase
 457 in F_N for 2017, but the distribution of $F_N/\langle F_N \rangle_{\tau=1\text{yr}}$ in Figure 5c is the same as for previous years.
 458 The overall distribution of $F_N/\langle F_N \rangle_{\tau=1\text{yr}}$ (Figure 4d) is much narrower than that for either
 459 $F_B/\langle F_B \rangle_{\tau=1\text{yr}}$ or $F_V/\langle F_V \rangle_{\tau=1\text{yr}}$ and has here been fitted with a lognormal of mean unity and
 460 variance $\nu = 0.009$ (mauve line). For such a low variance-to-mean ratio, the lognormal
 461 distribution is very close to Gaussian. The RMS deviation of the fitted lognormal from the
 462 observed N/N_{max} distribution is $\delta_{N,\text{logn}} = 2.6 \times 10^{-2}$ which is almost the same as that for F_B .

463 2.4 The effect of the IMF orientation

464 Figure 6 is the same as Figure 3 but for the term in P_α that depends on the IMF orientation, F_θ
 465 (equation 12). The shape of the distributions of both $F_\theta/[F_\theta]_o$ and $F_\theta/\langle F_\theta \rangle_{\tau=1\text{yr}}$ for this τ of 3
 466 hours is not well described by any of the standard parameterizations. Figure 2 of *Lockwood et*
 467 *al.* [2017] shows that this distribution evolves from having a singular and large peak at zero for τ
 468 = 5 min, into a lognormal form as τ increases to ≈ 6 hrs., which then falls in variance ν as τ
 469 further increases, becoming close to Gaussian for $\tau > 1$ day and a low-variance Gaussian tending
 470 to a delta function at unity as τ approaches 1 year. Figure 6a shows that there is a very slight
 471 variation in the distributions and means of $F_\theta/[F_\theta]_o$ but it does not follow the solar cycle and has
 472 almost completely been suppressed in $F_\theta/\langle F_\theta \rangle_{\tau=1\text{yr}}$ [*Stamper et al.*, 1999; *Lockwood*, 2003;
 473 *Lockwood et al.*, 2017].

474 2.5 The resulting distribution of P_α

475 Figure 7 is the same as Figure 3 but for the combination of these terms, P_α (equation 7). Given
 476 that the normalized factors in P_α ($F_B/\langle F_B \rangle_{\tau=1\text{yr}}$, $F_V/\langle F_V \rangle_{\tau=1\text{yr}}$, $F_N/\langle F_N \rangle_{\tau=1\text{yr}}$, and $F_\theta/\langle F_\theta \rangle_{\tau=1\text{yr}}$)
 477 all show very little year-to-year variation it is not surprising that neither does $P_\alpha/\langle P_\alpha \rangle_{\tau=1\text{yr}}$. The
 478 overall distribution shown in Figure 7d is quite close to a lognormal (the mauve line is the best
 479 fit with mean 1 and variance $\nu = 1.788$). Lognormal distributions arise when factors described
 480 by Gaussian or lognormal distributions are multiplied together. In this case, given that
 481 $F_B/\langle F_B \rangle_{\tau=1\text{yr}}$, $F_V/\langle F_V \rangle_{\tau=1\text{yr}}$, and $F_N/\langle F_N \rangle_{\tau=1\text{yr}}$ are described by three lognormal distributions (the
 482 last of which is of such low variance it is essentially Gaussian), so $F_B F_V F_N / \langle F_B F_V F_N \rangle_{\tau=1\text{yr}}$ is a
 483 (higher variance) lognormal.

484 However, the normalized IMF orientation factor $F_\theta/\langle F_\theta \rangle_{\tau=1\text{yr}}$ at $\tau = 3$ hrs does not follow a
 485 lognormal distribution and this has a major influence on the shape of the $P_\alpha/\langle P_\alpha \rangle_{\tau=1\text{yr}}$
 486 distribution. The RMS deviation of the fitted lognormal from the observed N/N_{max} distribution of
 487 P_α is $\delta_{P,\text{logn}} = 6.5 \times 10^{-2}$ which is roughly three times larger than that for F_B and F_N and twice that
 488 for F_V . Visual inspection of Figure 7d shows that the reason why this fit to the P_α distribution is

489 less good is that the lognormal distribution cannot match both the long tail of the observed
 490 distribution and the low mode value, which suggests a Weibull distribution. The best-fit Weibull
 491 distribution is described by a shape factor, k , of 1.0625, which with a scale factor, λ , of 1.0240
 492 gives the required mean of unity, and is shown by the blue line in Figure 7d. For this fit, the
 493 RMS deviation from the observed N/N_{\max} distribution for P_α is $\delta_{P,wb} = 6.4 \times 10^{-4}$ which is 1% of
 494 that for the lognormal distribution.

495 Hence we have established that the power input into the magnetosphere, normalized to its annual
 496 mean value, does not change greatly from year to year because the same is true for each of the
 497 terms that multiply together to form it. The shape of the overall distribution of P_α (at $\tau = 3$ hrs) is
 498 better fitted with a Weibull form than a lognormal form because of the influence of the IMF
 499 orientation factor F_θ . In the next section we study why, for $\tau = 3$ hrs., the P_α distribution has the
 500 form shown in Figures 7c and 7d. In comparing the relative widths of the factors in P_α , notice
 501 that the y-axis scales in Figures 4 -7 are different and have been chosen to show relative
 502 differences visually, yet also not suppress any small scale features. Note also that the constancy
 503 of the P_α distribution is not absolute but is a usable approximation (accuracies that are discussed
 504 in section 4). For example, we note that in Figure 4 there is an anomalous feature in the
 505 distribution of F_V in 2003 and in Figure 6 there is an anomalous feature in F_θ in the same year.
 506 Figure 7 shows that this does percolate through to an anomaly (albeit of smaller magnitude) in
 507 the distribution of P_α for this year.

508 3. The origins of the magnetospheric power input distribution

509 Figure 8 studies the evolution of the distributions of $P_\alpha / \langle P_\alpha \rangle_{\tau=1yr}$ and of the factors $F_B / \langle F_B \rangle_{\tau=1yr}$,
 510 $F_V / \langle F_V \rangle_{\tau=1yr}$, $F_N / \langle F_N \rangle_{\tau=1yr}$, and $F_\theta / \langle F_\theta \rangle_{\tau=1yr}$ with averaging timescale τ between 1 minute and
 511 3 hours. In each panel, the probability density function is color-coded as a function of the
 512 normalized parameter (vertical axis) and averaging timescale τ (horizontal axis). Panels (b), (d)
 513 and (e) (for, respectively, $F_B / \langle F_B \rangle_{\tau=1yr}$, $F_V / \langle F_V \rangle_{\tau=1yr}$, and $F_N / \langle F_N \rangle_{\tau=1yr}$) show that the
 514 distributions of normalized terms in F_B , F_V and F_N hardly change at all between $\tau = 1$ min. and

515 $\tau = 3$ hrs., and so the plots shown in Figures 3d, 4d and 5d apply, to a good degree of
 516 approximation, to all timescales below 3hrs (at least down to the 1 min limit studied here). On
 517 the other hand, Figure 8a shows that the distribution of the normalized power input P_α does
 518 change considerably over this range of τ , and Figure 8c shows that this change for P_α in large
 519 part mirrors that for the IMF orientation factor F_θ . At $\tau = 1$ min., the distribution is dominated by
 520 a very large number of zero and near-zero F_θ samples and, because F_θ appears as a multiplicative
 521 term in Equation (8), this generates a very large number of zero and near-zero P_α samples. For
 522 both $P_\alpha / \langle P_\alpha \rangle_{\tau=1\text{yr}}$ and $F_\theta / \langle F_\theta \rangle_{\tau=1\text{yr}}$, the distributions evolve in accordance with the central limit
 523 theorem [Heyde, 2006; Fischer, 2011], as discussed in Paper 3 [Lockwood *et al.*, 2018c].

524 Figure 2g shows that for $\tau = 1$ min. there is a secondary peak in the occurrence of values of $R =$
 525 $\log_{10}(\langle F_\theta \rangle_{1\text{min}} / \langle F_\theta \rangle_{1\text{yr}})$ around R of 0.45 associated with IMF orientations close to southward
 526 (explained below by Figure 9 and associated text). This peak is smaller in magnitude but broader
 527 than the corresponding one for R near -1 because of the $\sin^4(\theta_{\text{GSM}}/2)$ function used for F_θ . This
 528 feature is off-scale in Figure 8c which plots $\langle F_\theta \rangle_\tau / \langle F_\theta \rangle_{1\text{yr}}$ (i.e. on a linear scale rather than the
 529 logarithmic scale of R) as a function of τ . Rather than expand the scale in all panels of Figure 8
 530 and lose important detail, in Figure S14 of Part 4 of the Supporting Information we repeat
 531 Figures 8a and Figure 8c on a y-axis doubled length and scale which enables us to see this
 532 feature and track its evolution with τ . The feature is seen in S14(b) at $\langle F_\theta \rangle_\tau / \langle F_\theta \rangle_{1\text{yr}} \approx 2.8$ and τ
 533 $= 1$ min. As the averaging timescale is increased it disperses and moves towards average values
 534 for the same reasons that the large peak at $\langle F_\theta \rangle_{1\text{min}} / \langle F_\theta \rangle_{1\text{yr}} \approx 0$ disperses and moves towards
 535 average values, namely intervals of prolonged strongly southward and northward IMF become
 536 rarer as τ increases.

537 Hence the key to understanding the distribution for P_α at $\tau = 3$ hr. is understanding the
 538 distribution of $F_\theta = \sin^4(\theta_{\text{GSM}}/2)$ at $\tau = 1$ min. This investigated by Figure 9 which shows the
 539 distributions of one-minute averages of various IMF parameters. There are 10207789 valid
 540 1minute samples of the IMF and its components obtained in the years 1996-2016 (inclusive) – an
 541 availability of 92.4%. Figure 9a shows the distribution for the IMF B_Y component in the GSM
 542 frame, $[B_Y]_{\text{GSM}}$; Figure 9b for the IMF B_Z component, $[B_Z]_{\text{GSM}}$; and Figure 9c for the ratio,

543 $[B_Y]_{\text{GSM}}/[B_Z]_{\text{GSM}}$. The arctangent of this ratio is IMF clock angle in the GSM frame, $\theta_{\text{GSM}} =$
544 $\arctan([B_Y]_{\text{GSM}}/[B_Z]_{\text{GSM}})$, the distribution of which is shown in Figure 9d. Figure 9d shows that
545 IMF pointing due north ($[B_Y]_{\text{GSM}} = 0$, $[B_Z]_{\text{GSM}} > 0$, $\theta_{\text{GSM}} = 0$) is as common as IMF pointing due
546 south ($[B_Y]_{\text{GSM}} = 0$, $[B_Z]_{\text{GSM}} < 0$, $\theta_{\text{GSM}} = 180^\circ$), but IMF in the GSM equatorial plane ($[B_Z]_{\text{GSM}} =$
547 0 , $\theta_{\text{GSM}} = 90^\circ$) is twice as common. Figure 9e demonstrates what happens when the clock angle
548 is divided by 2 and convolved with a sine function in $\sin(\theta_{\text{GSM}}/2)$: the directly northward case
549 gives $\sin(\theta_{\text{GSM}}/2) = 0$, the directly southward IMF gives $\sin(\theta_{\text{GSM}}/2) = 1$, and $[B_Z]_{\text{GSM}} = 0$ gives
550 $\sin(\theta_{\text{GSM}}/2) \approx 0.71$. Note that the distribution becomes less smooth than the distribution of θ_{GSM} ,
551 which is the combined effect of binning the data into equal-width bins of $\sin(\theta_{\text{GSM}}/2)$ and of
552 $\sin(\theta_{\text{GSM}}/2)$ being a non-linear function of θ_{GSM} . What is not intuitive is what has happened to
553 the occurrence frequency of these values. The distribution in Figure 9e is dominated by the shape
554 of the sine function, the slope of which approaches 1 when $\theta_{\text{GSM}}/2 \rightarrow 0$ and approaches 0 when
555 $(\theta_{\text{GSM}}/2) \rightarrow 90^\circ$. This means that bins of equal width in $\sin(\theta_{\text{GSM}}/2)$ cover a smaller range of
556 θ_{GSM} at $\theta_{\text{GSM}}/2 \rightarrow 0$ (and so contain fewer samples), whereas they cover a larger range of θ_{GSM}
557 at $\theta_{\text{GSM}}/2 \rightarrow 90^\circ$ (and so contain a greater number of samples). This effect is convolved with the
558 distribution of samples with θ_{GSM} . This greatly reduces the number of samples with $\sin(\theta_{\text{GSM}}/2)$
559 near 0 (the quasi-northward IMF case) and greatly enhances the number of samples with
560 $\sin(\theta_{\text{GSM}}/2)$ near 1 (the quasi-southward IMF case). This can be seen in Figure 9e. Figure 9f
561 presents the distribution of $\sin^4(\theta_{\text{GSM}}/2)$ values. It can be seen that the peak near $\sin(\theta_{\text{GSM}}/2) = 0$
562 has been greatly enhanced whereas that near $\sin(\theta_{\text{GSM}}/2) = 1$ has been greatly diminished. The
563 reason is that raising to the 4th power moves values (which are all less than unity) towards zero.
564 The lowest bin of the histogram shown in figure 9f (for $\sin^4(\theta_{\text{GSM}}/2) < 0.02$) contains 18.94% of
565 all valid samples. For $\sin^2(\theta_{\text{GSM}}/2)$ the two peaks are of roughly the same magnitude (6.2% of
566 the samples are at $\sin^2(\theta_{\text{GSM}}/2) < 0.02$), and for $\sin^{8/3}(\theta_{\text{GSM}}/2)$ (as used by *Newell et al.* [2007])
567 the $\sin(\theta_{\text{GSM}}/2) \approx 0$ peak is greater than the $\sin(\theta_{\text{GSM}}/2) \approx 1$ peak, as in Figure 9f although to a
568 lesser extent (10.5% of the samples are at $\sin^{8/3}(\theta_{\text{GSM}}/2) < 0.02$). An insight into this distribution
569 of $\sin^4(\theta_{\text{GSM}}/2)$ is to compare it to an alternative IMF orientation factor that is often used, namely
570 B_s/B , where the southward field $B_s = -[B_Z]_{\text{GSM}}$ when $[B_Z]_{\text{GSM}} < 0$ and $B_s = 0$ when $[B_Z]_{\text{GSM}} \geq 0$.
571 This so-called ‘‘half-wave rectified’’ function means that all $[B_Z]_{\text{GSM}} > 0$ samples become zero in

572 B_S/B , and Figure 9b shows that this is true for half of the samples. Hence the distribution of B_S/B
 573 has an even larger peak at $\sin(\theta_{\text{GSM}}/2) \rightarrow 0$ (51.1% of samples are at $B_S/B < 0.02$). The
 574 distribution shown in Figure 9f is that shown by the vertical slice at the left-hand edge of Figure
 575 9c. It gives the distribution of $\langle P_\alpha \rangle_\tau / \langle P_\alpha \rangle_{\tau=1\text{yr}}$ for $\tau = 1\text{min}$ a form which, because of the Central
 576 Limit Theorem, evolves into the neo-Weibull distribution for $\langle P_\alpha \rangle_\tau / \langle P_\alpha \rangle_{\tau=1\text{yr}}$ at $\tau = 3\text{yr}$, as
 577 shown in Figure 8a. Because the distribution of $\langle P_\alpha \rangle_{\tau=1\text{min}} / \langle P_\alpha \rangle_{\tau=1\text{yr}}$ is set by that for
 578 $\langle F_\theta \rangle_{\tau=1\text{min}} / \langle F_\theta \rangle_{\tau=1\text{yr}}$ (with its dominant occurrence of zero or near-zero values) it is, to a large
 579 degree, the nature of solar-wind magnetosphere coupling that the coupling function has to
 580 capture, which predominantly defines the form of the power input distribution at $\tau = 1\text{min}$. As
 581 illustrated by Figures 8a and 8c, this also defines the form of the distributions at longer averaging
 582 timescales such as $\tau = 3\text{hours}$. Hence the shape of the distribution is set by the large variability
 583 of F_θ on short timescales and although variations in F_N , F_V , and F_B influence the mean value of
 584 P_α (and hence the PDF at every P_α value) they have very little effect on the shape of the
 585 distribution.

586 **4. Uncertainties caused by assuming the distribution of normalized power input is constant**

587 As mentioned previously, the result that the distribution of normalized power input into the
 588 magnetosphere is almost stationary is a very useful one. It has been used by *Lockwood et al.*
 589 [2017, 2018a] to predict the distributions of power input to the magnetosphere and of
 590 geomagnetic indices over the past 400 year from the annual means of solar wind parameters
 591 reconstructed by *Owens et al.* [2017]. The analysis carried out in the present paper gives us an
 592 opportunity to assess the accuracy of such applications of this result.

593 The blue lines in Figure 10a shows the PDFs, d , of $\langle P_\alpha \rangle_\tau / \langle P_\alpha \rangle_{\tau=1\text{yr}}$ for $\tau = 3\text{yr}$ for the 21
 594 individual years of the 1996-2016 period. (Note that, by definition, PDFs are normalized, the
 595 integral of each curve along the y-axis being unity). The black line is the mean and the orange
 596 area is between the mean plus and minus one standard deviation. Figure 10b shows the
 597 deviations from the mean, expressed as a percentage, $\delta_d = 100(d - \langle d \rangle) / \langle d \rangle$ and in the same
 598 formats as Figure 10a. The horizontal lines show the limits of the upper 1%, 5%, 10% and 20%

599 of the cumulative distribution function (CDF, see Figure 11). The $1-\sigma$ error in the PDF is below
 600 11% for the lower 80% of the $P_\alpha / \langle P_\alpha \rangle_{\tau=1\text{yr}}$ values (the error being $\pm 11\%$ for the 20% threshold),
 601 but rises to $\pm 14.5\%$ for the 10% threshold, $\pm 28\%$ for the 5% threshold and $\pm 57\%$ for the 1%.

602 However, for space weather applications we are not as interested in the probability of a given
 603 $\langle P_\alpha \rangle_\tau$ value as we are in the probability of $\langle P_\alpha \rangle_\tau$ exceeding a certain threshold: in other words
 604 we are more interested in the CDFs, c , than the PDFs, d . The CDFs are shown in Figure 11a,
 605 using the same format as Figure 10a and the errors in the mean CDF, $\delta_c = 100(c - \langle c \rangle) / \langle c \rangle$ are
 606 shown in Figure 11b. In this case, the $1-\sigma$ uncertainty in predicting an event in the top 20% of
 607 all events is $\pm 8.5\%$; in the top 10% of all events is $\pm 10\%$; in the top 5% of all events is $\pm 12\%$;
 608 and in the top 1% is $\pm 40\%$.

609 2. Conclusions

610 We have studied why the power input into the magnetosphere, P_α (averaged over intervals of
 611 duration $\tau = 3$ hours), follows the distribution that it does by looking at the component terms.
 612 We use the optimum coupling function $\alpha = 0.44$ which was shown in Paper 1 [Lockwood *et al.*,
 613 2018b] to apply at all timescales between 1 minute and 1 year for the geomagnetic index, with
 614 the most uniform response, *am*.

615 The solar wind mass density factor introduces the smallest variability into the P_α distribution (the
 616 variance/mean ratio for the distribution this factor being 0.009). The factors depending on the
 617 IMF magnitude and on the solar wind speed follow quasi lognormal distributions of similar
 618 shape (the variance/mean ratios being 0.120 and 0.127, respectively). These factors all contribute
 619 to the shape of the P_α distribution, but the dominant one is the IMF orientation factor. We have
 620 shown how this arises from the nature of the optimum coupling functions and the role magnetic
 621 reconnection in the dayside magnetopause (the reconnection voltage being strongly dependent on
 622 the orientation of the IMF vector). The distributions of the total mass density factor, the IMF
 623 magnitude factor and the solar wind speed factor hardly change between an averaging timescale
 624 of 1 minute and 3 hours, whereas the IMF orientation factor distribution changes rapidly. At $\tau =$

625 1 minute the distribution of the IMF orientation factor has a very large peak at near-zero values
 626 (see Figure 9f), which arises from the fact that for almost exactly half of all time the IMF points
 627 northward in the GSM frame (see Figure 9b) and so P_α is low. This peak is smoothed out as the
 628 averaging timescale as τ is increased (in accordance with the central limit theorem). As a result,
 629 the distribution of power input into the magnetosphere at any τ is set by the distribution of the
 630 IMF orientation factor at very high time resolution.

631 Given this great importance of the IMF orientation factor, it is sensible to check that we are using
 632 the best functional form in our analysis. A great many papers have deployed coupling functions
 633 using the form $\sin^n(\theta_{\text{GSM}})$, where θ_{GSM} is the IMF clock angle in the GSM frame, but the optimum
 634 exponent, n , has been estimated to be anything between zero and 6. The first coupling functions
 635 that allowed for IMF orientation were often referred to as “half wave rectifier” functions because
 636 they were set to zero the 50% of the time that the IMF had a northward component (see Figure
 637 9b) (a reference to the signal processing effect of software and devices that pass only one
 638 polarity of a parameter of the input signal into the output signal) [Burton *et al.*, 1975;
 639 Murayama, *et al.*, 1980]. Bargatze *et al.* [1986] point out that in terms of IMF orientation
 640 studies using half-wave rectified B_{ZM} are using a factor of the form $U(\theta_{\text{GSM}})\cos(\theta_{\text{GSM}})$ where
 641 θ_{GSM} is the IMF clock angle in the GSM frame and $U(\theta_{\text{GSM}}) = -1$ when $\theta_{\text{GSM}} \geq 90^\circ$ and $U(\theta_{\text{GSM}})$
 642 $= 0$ when $\theta_{\text{GSM}} < 90^\circ$. Because it is continuous in slope, and because it allows for the fact that
 643 low-latitude (between the cusps) magnetopause reconnection is not switched off whenever the
 644 IMF is northward [Chandler *et al.*, 1999], the $\sin^n(\theta_{\text{GSM}})$ function has generally been seen as
 645 preferable, from MHD magnetospheric modelling Hu *et al.* [2009] and Fedder *et al.* [2012] and
 646 found $n \approx 1$, but statistical estimates from observations vary from $n = 2$ [Kan and Lee, 1979;
 647 Doyle and Burke, 1983; Lyatsky *et al.*, 2007; Milan *et al.*, 2008], $n = 2.67$ [Newell *et al.*, 2007],
 648 $n = 4$ [Perreault and Akasofu, 1978; Wygant *et al.*, 1983; Scurry and Russell, 1991; Stamper *et*
 649 *al.*, 1999], $n = 4.5$ [Milan *et al.*, 2012], to $n = 6$ [Temerin and Li, 2006; Boynton *et al.*, 2011].
 650 The wide range in estimated n values may be because these studies employ different indicators
 651 of terrestrial disturbance but most studies employ interplanetary data with large data and many
 652 data gaps which, as shown by Paper 1, introduce considerable noise. The Supporting Information
 653 file contains an analysis of 20 years’ data of 1-minute auroral *SML* index values (the equivalent

654 of AL from the very extensive SuperMAG network of magnetometers) and interplanetary data
655 with few data gaps that are dealt with rigorously, as detailed in Paper 1. The results clearly
656 confirm that $\sin^4(\theta_{\text{GSM}})$ is indeed the best IMF orientation factor for use in P_α .

657 We have shown that the distribution of power input into the magnetosphere (normalized to its
658 annual mean value, i.e. of $\langle P_\alpha \rangle_{\tau=3\text{hr}} / \langle P_\alpha \rangle_{\tau=1\text{yr}}$) on an averaging timescale of $\tau = 3$ hrs., is a
659 Weibull distribution with $k = 1.0625$ and $\lambda = 1.0240$ (which yields the required mean of unity).
660 All the factors, when normalized to their annual mean value, show annual distributions which
661 vary only slightly from year to year. Hence the multiplicative product of these factors, the power
662 input to the magnetosphere, also behaves this way.

663 We have studied the uncertainties inherent in using the fact that the normalized power input (and
664 hence the geomagnetic activity indices that correlate highly with it) has a distribution of almost
665 constant shape and variance. For the number of events in the largest 10% the one-sigma error is
666 10% and for events in the largest 5% the one-sigma error is 12%. Hence the probabilities given
667 in the space climatological study by *Lockwood et al.* [2018a] (which were in the largest 5% and
668 based on reconstructed annual means) have an uncertainty of 12%, which has to be convolved
669 with the uncertainty in the reconstructed mean value. Moving to the more extreme events, we
670 show that the uncertainty in using the constant shape distribution rises to 40% for the top 1% of
671 events. This stresses the unsuitability of this approach for the most extreme events and the fact
672 that the extreme tail of the distribution may show a different form and that this tail can vary in
673 ways different to the bulk of the distribution [e.g. *Vörös et al.*, 2015]. Studies of extreme events
674 in the tail of the distribution will be discussed in later papers, but here we study the bulk of the
675 distribution and stress that the results, although useful for defining the occurrence of “large and
676 extreme events” (for example in in the top 5% of the overall occurrence distribution), cannot be
677 extended to cover the most extreme events without the use of Extreme Value Statistics (EVS).

678 In paper 3 of this series [*Lockwood et al.*, 2018s] we will study the how the distributions of
679 power input into the magnetosphere and of geomagnetic indices continue to evolve with
680 averaging timescale τ between 3 hours and 1 year. The reason this is of interest to the

681 development of a space weather climatology is because several studies have shown that many
682 geomagnetic storms are the response to the time-integrated solar wind forcing over an extended
683 period [Echer et al., 2008; Turner et al., 2009; Lockwood et al., 2016; Mourenas et al., 2018]
684 and also the time-integration of the geomagnetic activity response is important for space weather
685 phenomena such as GICs (Geomagnetically Induced Currents) in systems like power grids
686 [Gaunt and Coetzee, 2007; Ramírez-Niño et al., 2016] and the growth of energetic particles that
687 can be damaging or disruptive to spacecraft electronics [Mourenas et al., 2018]. Using solar
688 wind power input P_α as a metric, integrated forcing over an interval of duration τ is $\tau \times \langle P_\alpha \rangle_\tau$.
689 However, we note that $\tau \times \langle P_\alpha \rangle_\tau$ (or the time integral of another form of coupling function) is
690 unlikely to be a fully adequate predictor because preconditioning or multiple events may be
691 factors [see discussion by Lockwood et al., 2016] as may impulsive events, such as sudden
692 increases in solar wind speed [Balan et al., 2017]. Furthermore, it is not yet clear what timescale
693 τ is most relevant to a given phenomenon. Figure 6 of Wygant et al. [1983] is significant because
694 it shows that it can take of order 10 hours following a northward turning to return transpolar
695 voltage to its baselevel values, which implies 4 or 5 substorms are required to reduce excess
696 open flux (i.e. energy stored in the tail) even though the IMF is northward. Periods of northward
697 IMF of 10 hrs. duration or more are rare [Hapgood et al., 1991] and so it is likely that southward
698 IMF will drive renewed energy storage in the tail before the magnetosphere has returned to a
699 quiet state. Kamide et al. [1977] showed that although substorms were more common when the
700 IMF pointed southward, they do occur during northward IMF if the polar cap was large
701 (indicating large open flux and hence high energy storage in the tail) and Lee et al. [2010] show
702 that substorms during northward IMF driven by stored tail energy can be as strong as events
703 during southward IMF. The ability of the tail to accumulate stored energy means that longer
704 periods of solar wind forcing have the potential drive extremely large events, even if the forcing
705 is intermittent and bursty on shorter timescales. Lockwood et al. [2016] estimate that the
706 relevant τ may be as large as 4-5 days.

707 **Acknowledgments and Data**

708 The authors are grateful to the staff of Space Physics Data Facility, NASA/Goddard Space Flight
709 Centre, who prepared and made available the OMNI2 dataset used. The data were downloaded
710 from <http://omniweb.gsfc.nasa.gov/ow.html>. The work presented in this paper is supported by
711 STFC consolidated grant number ST/M000885/1 and the work of ML and MJO is also supported

712 by the SWIGS NERC Directed Highlight Topic Grant number NE/P016928/1/ and OA by
 713 NERC Grant NE/P017274/1. SB is supported by an NERC PhD studentship.

714

715 **References**

- 716 Asvestari, E. I.G. Usoskin, G.A. Kovaltsov, M.J. Owens, N.A. Krivova, S. Rubinetti and C.
 717 Taricco (2017) Assessment of different sunspot number series using the cosmogenic
 718 isotope ^{44}Ti in meteorites, *Mon. Not. R. Astron. Soc.*, **467** (2), 1608-1613, doi:
 719 10.1093/mnras/stx190
- 720 Asvestari, E., and I. G. Usoskin (2016) An empirical model of heliospheric cosmic ray
 721 modulation on long-term time scale, *J. Space Weather Space Clim.*, **6**, A15, doi:
 722 10.1051/swsc/2016011
- 723 Badruddin, and O.P.M. Aslam (2013) Study of the solar wind-magnetosphere coupling on
 724 different time scales, *Planet. Space Sci.*, **85**, 123-141, doi: 10.1016/j.pss.2013.06.006
- 725 Balan, N., Y. Ebihara, R. Skoug, K. Shiokawa, I. S. Batista, S. Tulasi Ram, Y. Omura, T.
 726 Nakamura, and M.-C. Fok (2017) A scheme for forecasting severe space weather.
 727 *Journal of Geophysical Research: Space Physics*, **122**, 2824-2835, doi:
 728 10.1002/2016JA023853
- 729 Balogh, A., T.J. Beek, R.J. Forsyth, P.C. Hedgecock, R.J. Marquedant, E.J. Smith, D.J.
 730 Southwood, and B.T. Tsurutani, The magnetic field investigation on the Ulysses mission-
 731 Instrumentation and preliminary scientific results, *Astron. and Astrophys Supplement*
 732 *Series*, 92 (2), 221-223, 1992, ISSN: 0365-0138
- 733 Bargatze, L.F.B., R. L. McPherron, D. N. Baker (1986) Solar Wind-Magnetosphere Energy Input
 734 Functions, in *Solar Wind-Magnetosphere Coupling*. Eds, Y. Kamide, J.A. Slavin, Terra
 735 Scientific Publishing Company, Tokyo, Japan, and D. Reidel Publishing Company,
 736 Dordrecht, Holland, ISBN: 90-277-2303-6, pp. 101-109, doi: 10.1007/978-94-009-4722-
 737 1_7.
- 738 Bartels, J., Heck, N.H. and Johnston, H.F. (1939) The three-hour-range index measuring
 739 geomagnetic activity, *Terr. Magn. Atmos. Electr.*, 44, 411–454, doi:
 740 10.1029/TE044i004p00411
- 741 Boynton, R. J., M. A. Balikhin, S. A. Billings, H. L. Wei, and N. Ganushkina (2011), Using the
 742 NARMAX OLS-ERR algorithm to obtain the most influential coupling functions that
 743 affect the evolution of the magnetosphere, *J. Geophys. Res.*, **116**, A05218,
 744 doi:10.1029/2010JA015505.
- 745 Burton, R. K., R. L. McPherron, and C. T. Russell (1975) An empirical relationship between
 746 interplanetary conditions and Dst, *J. Geophys. Res.*, **80** (31), 4204–4214, doi:
 747 10.1029/JA080i031p04204
- 748 Chandler, M.O., S.A. Fuselier, M. Lockwood and T.E. Moore (1999) Evidence of component
 749 magnetic merging equatorward of the cusp, *J. Geophys. Res.*, **104**, 22623-22648, doi:
 750 10.1029/1999JA900175
- 751 Cliver, E.W., V. Boriakoff, and K. H. Bounar (1996) The 22-year cycle of geomagnetic activity,
 752 *J. Geophys. Res.*, **101**, 27091–27109, doi: 10.1029/96ja02037

- 753 Demetrescu, C., V. Dobrica, and G. Maris (2010) On the long-term variability of the heliosphere-
 754 magnetosphere environment, *Adv. Space Res.*, **46** (10), 1299-1312, doi:
 755 10.1016/j.asr.2010.06.032
- 756 Doyle, M. A., and W. J. Burke (1983) S3-2 measurements of the polar cap potential, *J. Geophys.*
 757 *Res.*, **88** (11), 9125-9133, doi: 10.1029/ja088ia11p09125
- 758 Echer, E., W. D. Gonzalez, and B. T. Tsurutani (2008), Interplanetary conditions leading to
 759 superintense geomagnetic storms (Dst > 250 nT) during solar cycle 23, *Geophys. Res.*
 760 *Let.*, **35**, L06S03, doi:10.1029/2007GL031755.
- 761 Farrugia, C.J., M.P. Freeman, S.W.H. Cowley, D.J. Southwood, M. Lockwood and A. Etemadi
 762 (1989) Pressure-driven magnetopause motions and attendant response on the ground,
 763 *Planet. Space Sci.*, **37**, 589-608, doi: 10.1016/0032-0633(89)90099-8
- 764 Fedder, J.A., C.M. Mobarry, J.G. Lyon (2012) Reconnection voltage as a function of IMF clock
 765 angle, *Geophys. Res. Let.*, **18** (6), 1047-1050, doi:10.1029/90GL02722
- 766 Feynman, J. and N. U. Crooker (1978) The solar wind at the turn of the century, *Nature*, **275**,
 767 626 – 627, doi: 10.1038/275626a0
- 768 Finch, I.D. (2008) The use of geomagnetic activity observations in studies of solar
 769 windmagnetosphere coupling and centennial solar change, *PhD thesis, University of*
 770 *Southampton*, British Library Ethos ID: uk.bl.ethos.485008
- 771 Finch, I.D., and M. Lockwood (2007), Solar wind-magnetosphere coupling functions on
 772 timescales of 1 day to 1 year, *Annales Geophys.*, **25**, 495-506, doi: 10.5194/angeo-25495-
 773 2007
- 774 Finlay C.C., S. Maus, C.D. Beggan, T.N. Bondar, A. Chambodut, T.A. Chernova, A. Chulliat,
 775 V.P. Golovkov, B. Hamilton, M. Hamoudi, R. Holme, G. Hulot, W. Kuang, B. Langlais,
 776 V. Lesur, F.J. Lowes, H. Lühr, S. Macmillan, M. Manda, S. McLean, C. Manoj, M.
 777 Menvielle, I. Michaelis, N. Olsen, J. Rauberg, M. Rother, T.J. Sabaka, A. Tangborn, L.
 778 Tøffner-Clausen, E. Thébault, A.W.P. Thomson, I. Wardinski, Z. Wei, T.I. Zvereva
 779 (2010) International Geomagnetic Reference Field: the eleventh generation, *Geophys. J.*
 780 *Int.*, **183**, 1216–1230, doi: 10.1111/j.1365-246X.2010.04804.x.
- 781 Fischer, H. (2011) A History of the Central Limit Theorem, from Classical to Modern
 782 Probability Theory, book in series “*Sources and Studies in the History of Mathematics*
 783 *and Physical Sciences*”, Springer, New York, doi:10.1007/978-0-387-87857-7
- 784 Gaunt, C.T. and G. Coetzee (2007) Transformer failures in regions incorrectly considered to
 785 have low GIC-risk, in *2007 IEEE Lausanne Power Tech*, Lausanne, Switzerland, 1-5
 786 July 2007, pp 807-812, doi: 10.1109/PCT.2007.4538419
- 787 Hapgood, M.A., G. Bowe, M. Lockwood, D.M. Willis, and Y. Tulunay (1991) Variability of the
 788 interplanetary magnetic field at 1 A.U. over 24 years: 1963 – 1986, *Planet. Space Sci.*,
 789 **39**, 411-423, doi: 10.1016/0032-0633(91)90003-S
- 790 Heyde, C. (2006) Central Limit Theorem, in *Encyclopedia of Actuarial Science*, 1, John Wiley
 791 and Sons, doi: 10.1002/9780470012505.tac019

- 792 Holappa, L., K. Mursula, and T. Asikainen (2014) A new method to estimate annual solar wind
793 parameters and contributions of different solar wind structures to geomagnetic activity, *J.*
794 *Geophys. Res. Space Physics*, **119**, 9407–9418, doi: 10.1002/2014JA020599
- 795 Hu, Y.Q., Z. Peng, C. Wang, J.R. Kan (2009) Magnetic merging line and reconnection voltage
796 versus IMF clock angle: Results from global MHD simulations, *J. Geophys. Res.*, **114**,
797 (8), A08220, doi:10.1029/2009JA014118
- 798 Kan, J. R. and Lee, L. C. (1979) Energy coupling function and solar wind-magnetosphere
799 dynamo, *Geophys. Res. Lett.*, **6**, 577-580. doi:10.1029/GL006i007p00577
- 800 Karoff, C., F. Inceoglu, M. F. Knudsen, J. Olsen and A. Fogtman-Schulz, The lost sunspot
801 cycle: New support from ¹⁰Be measurements, *Astron. and Astrophys.*, **575**, A77, doi:
802 10.1051/0004-6361/201424927
- 803 Kamide, Y., P. D. Perreault, S-I. Akasofu, and J. D. Winningham (1977) Dependence of
804 substorm occurrence probability on the interplanetary magnetic field and on the size of
805 the auroral oval, *Journal of Geophysical Research* 82, (35), 5521-5528, doi:
806 10.1029/ja082i035p05521
- 807 Kataoka, R., H. Isobe, H. Hayakawa, H. Tamazawa, A.D. Kawamura, H. Miyahara, K. Iwahashi,
808 K. Yamamoto, M. Takei, T. Terashima, H. Suzuki, Y. Fujiwara and T. Nakamura (2017),
809 Historical space weather monitoring of prolonged aurora activities in Japan and in China,
810 *Space Weather*, **15**, 392–402, doi:10.1002/2016SW001493.
- 811 Koyama, Y., A. Shinbori, Y. Tanaka, T. Hori, M. Nosé, and S. Oimatsu (2014) An Interactive
812 Data Language software package to calculate ionospheric conductivity by using
813 numerical models, *Computer Phys. Comms.*, **185** (12), 3398-3405, doi:
814 10.1016/j.cpc.2014.08.011
- 815 Lean, J., Y.-M. Wang, and N.R. Sheeley Jr. (2002) The effect of increasing solar activity on the
816 Sun's total and open magnetic flux during multiple cycles: Implications for solar forcing
817 of climate, *Geophys. Res. Lett.*, **29** (24), 2224, doi: 10.1029/2002GL015880
- 818 Lee, D.-Y., K.-C. Choi, S. Ohtani, J. H. Lee, K. C. Kim, K. S. Park, and K.-H. Kim (2010) Can
819 intense substorms occur under northward IMF conditions?, *J. Geophys. Res.*, **115**, A01211,
820 doi:10.1029/2009JA014480.
- 821 Legrand, J.-P. and P.A. Simon (1987) Two hundred years of auroral activity (1780-1979),
822 *Annales Geophys.*, **A5**, 161-167.
- 823 Lockwood, M. (2003) Twenty-three cycles of changing open solar flux, *J. Geophys. Res.*, **108**
824 (A3), 1128, doi: 10.1029/2002JA009431
- 825 Lockwood, M. (2013) Reconstruction and Prediction of Variations in the Open Solar Magnetic
826 Flux and Interplanetary Conditions, *Living Rev. Solar Physics*, **10**, 4, 2013. doi:
827 10.12942/lrsp-2013-4
- 828 Lockwood, M. and L. Barnard (2015) An arch in the UK: a new catalogue of auroral
829 observations made in the British Isles and Ireland, *Astron. and Geophys.*, **56** (4),
830 4.254.30, doi: 10.1093/astroph/atv132

- 831 Lockwood, M. and M. Owens (2009) The accuracy of using the Ulysses result of the spatial
832 invariance of the radial heliospheric field to compute the open solar flux, *Ap. J.*, **701** (2),
833 964-973, doi: 10.1088/0004-637X/701/2/964, 2009
- 834 Lockwood, M. and M.J. Owens (2011) Centennial changes in the heliospheric magnetic field and
835 open solar flux: the consensus view from geomagnetic data and cosmogenic isotopes and
836 its implications, *J. Geophys. Res.*, **116**, A04109, doi: 10.1029/2010JA016220
- 837 Lockwood, M., and M.J. Owens (2014a) Centennial variations in sunspot number, open solar
838 flux and streamer belt width: 3. Modelling, *J. Geophys. Res. Space Physics*, **119** (7),
839 5193–5209, doi: 10.1002/2014JA019973
- 840 Lockwood, M. and M.J. Owens (2014b) Implications of the recent low solar minimum for the
841 solar wind during the Maunder minimum, *Astrophys. J. Lett.*, 781:L7, doi:
842 10.1088/20418205/781/1/L7
- 843 Lockwood, M., R. Stamper and M.N. Wild (1999) A doubling of the sun's coronal magnetic field
844 during the last 100 years, *Nature*, **399**, 437-439, doi: 10.1038/20867
- 845 Lockwood, R.B. Forsyth, A. Balogh, and D. J. McComas (2004) Open solar flux estimates from
846 near-Earth measurements of the interplanetary magnetic field: comparison of the first two
847 perihelion passes of the Ulysses spacecraft, *Annales Geophys.*, **22**, 1395-1405, doi:
848 10.5194/angeo-22-1395-2004
- 849 Lockwood, M., A.P. Rouillard, I.D. Finch, and R (2006) Comment on "The IDV index: its
850 derivation and use in inferring long-term variations of the interplanetary magnetic field
851 strength" by Svalgaard and Cliver, *J. Geophys. Res.*, 111, A09109,
852 doi:10.1029/2006JA011640
- 853 Lockwood, M. Owens, and A.P. Rouillard (2009a) Excess Open Solar Magnetic Flux from
854 Satellite Data: I. Analysis of the 3rd Perihelion Ulysses Pass, *J. Geophys. Res.*, **114**,
855 A11103, doi:10.1029/2009JA014449
- 856 Lockwood, M., M. Owens, and A. P. Rouillard (2009b) Excess open solar magnetic flux from
857 satellite data: 2. A survey of kinematic effects, *J. Geophys. Res.*, 114, A11104, doi:
858 10.1029/2009JA014450.
- 859 Lockwood, M., H. Nevanlinna, L. Barnard, M.J. Owens, R.G. Harrison, A.P. Rouillard, and C.J.
860 Scot (2014a) Reconstruction of Geomagnetic Activity and Near-Earth Interplanetary
861 Conditions over the Past 167 Years: 4. Near-Earth Solar Wind Speed, IMF, and Open
862 Solar Flux, *Annales. Geophys.*, **32**, 383-399, doi:10.5194/angeo-32-383-2014
- 863 Lockwood, M., M.J. Owens, E. L.A. Barnard, and I.G. Usoskin (2016a) An assessment of
864 sunspot number data composites over 1845-2014, *Astrophys. J.*, **824**, 54, doi:
865 10.3847/0004-637X/824/1/54
- 866 Lockwood, M., M.J. Owens, L.A. Barnard S. Bentley, C.J. Scott, and C.E. Watt (2016b) On the
867 Origins and Timescales of Geoeffective IMF, *Space Weather*, **14**, 406–432, doi:
868 10.1002/2016SW001375
- 869 Lockwood, M., M.J. Owens, L.A. Barnard, C.J. Scott, and C.E. Watt (2017) Space Climate and
870 Space Weather over the past 400 years: 1. The Power input to the Magnetosphere, *J.*
871 *Space Weather Space Clim.*, **7**, A25, doi: 10.1051/swsc/2017019.

- 872 Lockwood, M., M.J. Owens, L.A. Barnard, C.J. Scott, C.E. Watt and S. Bentley (2018a) Space
 873 Climate and Space Weather over the past 400 years: 2. Proxy indicators of geomagnetic
 874 storm and substorm occurrence, *J. Space Weather Space Clim.*, in press, doi:
 875 10.1051/swsc/2017048
- 876 Lockwood, M., S. Bentley, M.J. Owens, L.A. Barnard, C.J. Scott, C.E. Watt and O. Allanson
 877 (2018b) The development of a space climatology: 1. Solar-wind magnetosphere coupling
 878 as a function of timescale and the effect of data gaps, *Space Weather*, in press, doi:
 879 10.1029/2018SW001856
- 880 Lockwood, M., S. Bentley, M.J. Owens, L.A. Barnard, C.J. Scott, C.E. Watt and O. Allanson
 881 (2018c) The development of a space climatology: 3. The evolution of distributions of
 882 space weather parameters with timescale, *Space Weather*, submitted with current paper
- 883 Lyatsky, W., S. Lyatskaya, and A. Tan (2007) A coupling function for solar wind effect on
 884 geomagnetic activity, *Geophys. Res. Lett.*, **34**, L02107, doi: 10.1029/2006GL027666.
- 885 Mackay, D.H. and M. Lockwood (2002) The Evolution of the Sun's Open magnetic Flux: II. Full
 886 solar cycle simulations, *Solar Phys.*, 209 (2), 287-309, doi: 10.1023/A:1021230604497
- 887 Mackay, D.H., E. R. Priest, and M. Lockwood (2002) The Evolution of the Sun's Open Magnetic
 888 Flux: I. A Single Bipole, *Solar Phys.*, **207** (2), 291-308, doi: 10.1023/A:1016249917230,
 889 2002
- 890 Matthes, K., B. Funke, M.E.Andersson, L. Barnard, J. Beer, P. Charbonneau, M.A. Clilverd, T.
 891 Dudok de Wit, M. Haberreiter, A. Hendry, C.H. Jackman, M. Kretzschmar, T. Kruschke,
 892 M. Kunze, U. Langematz, D.R. Marsh, A. Maycock, S. Misios, C.J. Rodger, A.A. Scaife,
 893 A. Seppälä, M. Shanguan, M. Sinnhuber, K. Tourpali, I. Usoskin, M. van de Kamp, P.T.
 894 Verronen, and S.Versick (2017) Solar Forcing for CMIP6 (v3.1), *Geosci. Model Dev.*,
 895 10, 2247-2302, doi: 10.5194/gmd-2016-91
- 896 Milan, S. E., J. S. Gosling, and B. Hubert (2012), Relationship between interplanetary parameters
 897 and the magnetopause reconnection rate quantified from observations of the expanding
 898 polar cap, *J. Geophys. Res.*, **117**, A03226, doi: 10.1029/2011JA017082.
- 899 Milan, S. E., P. D. Boakes, and B. Hubert (2008) Response of the expanding/contracting polar
 900 cap to weak and strong solar wind driving: Implications for substorm onset, *J. Geophys.*
 901 *Res.*, 113, A09215, doi:10.1029/2008JA013340.
- 902 Mourenas, D., A.V. Artemyev, and X.-J. Zhang (2018), Statistics of extreme time integrated
 903 geomagnetic activity, *Geophysical Research Letters*, **45**, 502-510, doi:
 904 10.1002/2017GL076828
- 905 Murayama, T., T. Aoki, H. Nakai, and K. Hakamada (1980) Empirical formula to relate the
 906 auroral electrojet intensity with interplanetary parameters, *Planet. Space Sci.*, 28, 803-
 907 813, doi: 10.1016/0032-0633(80)90078-1
- 908 Nagatsuma, T. (2006) Diurnal, semiannual, and solar cycle variations of solar wind
 909 magnetosphere-ionosphere coupling, *J. Geophys. Res.*, **111**, A09202, doi:
 910 10.1029/2005JA011122

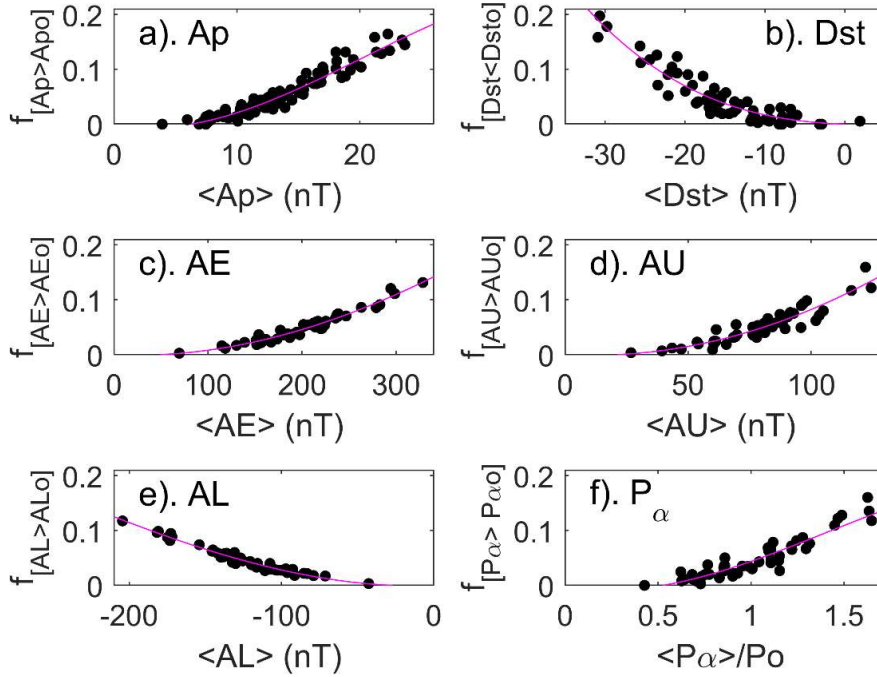
- 911 Newell, P.T., T. Sotirelis, K. Liou, C.-I. Meng, and F. J. Rich (2007) A nearly universal solar
 912 wind-magnetosphere coupling function inferred from 10 magnetospheric state variables,
 913 *J. Geophys. Res.*, **112**, A01206, doi:10.1029/2006JA012015.
- 914 Owens, M. J., C.N. Arge, N.U. Crooker, N.A. Schwadron, and T.S. Horbury (2008), Estimating
 915 total heliospheric magnetic flux from single-point in situ measurements, *J. Geophys. Res.*,
 916 **113**, A12103, doi: 10.1029/2008JA013677
- 917 Owens, M. J., Lockwood, M., Riley, P., & Linker, J. (2017). Sunward strahl: A method to
 918 unambiguously determine open solar flux from in situ spacecraft measurements using
 919 suprathermal electron data. *Journal of Geophysical Research: Space Physics*, **122**, doi:
 920 10.1002/2017JA024631
- 921 Owens, M.J. and M. Lockwood (2012) Cyclic loss of open solar flux since 1868: The link to
 922 heliospheric current sheet tilt and implications for the Maunder Minimum, *J. Geophys.*
 923 *Res.*, **117**, A04102, doi:10.1029/2011JA017193.
- 924 Owens, M.J., E. Cliver, K. McCracken, J. Beer, L.A. Barnard, M. Lockwood, A.P. Rouillard, D.
 925 Passos, P. Riley, I.G. Usoskin, Y.-M. Wang (2016a) Near-Earth Heliospheric Magnetic
 926 Field Intensity since 1800. Part 1: Sunspot and Geomagnetic Reconstructions, *J.*
 927 *Geophys. Res.*, **121** (7), 6048-6063, doi: 10.1002/2016JA022529
- 928 Owens, M.J., E. Cliver, K. McCracken, J. Beer, L.A. Barnard, M. Lockwood, A.P. Rouillard, D.
 929 Passos, P. Riley, I.G. Usoskin, Y.-M. Wang (2016b) Near-Earth Heliospheric Magnetic
 930 Field Intensity since 1800. Part 2: Cosmogenic Radionuclide Reconstructions, *J.*
 931 *Geophys. Res.*, **121** (7), 6064-6074, doi: 10.1002/2016JA022550
- 932 Owens, M.J., M. Lockwood, and P. Riley (2017) Global solar wind variations over the last four
 933 centuries, *Nature Scientific Reports*, **7**, Article number 41548, doi: 10.1038/srep41548
- 934 Owens, M.J., N.U. Crooker, and M. Lockwood, How is open solar magnetic flux lost over the
 935 solar cycle?, *J. Geophys. Res.*, **116**, A04111, 2011, doi: 10.1029/2010JA016039, 2011
- 936 Perreault, P. and Akasofu, S. (1978), A study of geomagnetic storms. *Geophys. J. Roy. Astron.*
 937 *Soc.*, **54**, 547-573. doi:10.1111/j.1365-246X.1978.tb05494.x
- 938 Ramírez-Niño, J., C. Haro-Hernández, J. HéctorRodríguez-Rodríguez, R. Mijarez (2016) Core
 939 saturation effects of geomagnetic induced currents in power transformers, *Journal of*
 940 *Applied Research and Technology*, **14**, (2), 87-92, doi: 10.1016/j.jart.2016.04.003.
- 941 Rahmanifard F., N.A. Schwadron, C.W. Smith, K.G. McCracken, K.A. Duderstadt, N.Lugaz,
 942 and M.L. Goelzer (2017) Inferring the Heliospheric Magnetic Field Back through
 943 Maunder Minimum, *Astrophys. J.*, **837** (2), 165/1-165/14, doi: 10.3847/15384357/aa6191
- 944 Redner, S. (1990) Random multiplicative processes: an elementary tutorial, *Am. J. Phys.*,
 945 **58** (3), 267-273, doi: 10.1119/1.16497
- 946 Riley, P., and J. J. Love (2017) Extreme geomagnetic storms: Probabilistic forecasts and their
 947 uncertainties, *Space Weather*, **15**, 53–64, doi: 10.1002/2016SW001470
- 948 Roelof, E.C. and D.G. Sibeck (1993) Magnetopause shape as a bivariate function of
 949 interplanetary magnetic field Bz and solar wind dynamic pressure. *Journal of*
 950 *Geophysical Research: Space Physics*, **98** (A12), pp.21421-21450, doi:
 951 10.1029/93ja02362

- 952 Rouillard, A.P., M. Lockwood and I.D. Finch (2007) Centennial changes in the solar wind speed
953 and in the open solar flux. *J. Geophys. Res.*, **112**, A05103, doi: 10.1029/2006JA012130.
- 954 Schrijver, C.J., M.L. DeRosa, and A.M. Title (2002) What is missing from our understanding of
955 long-term solar and Heliospheric activity?, *Astrophys. J.*, **577**, 1006–1012, doi:
956 10.1086/342247
- 957 Scurry, L., and C. T. Russell (1991), Proxy studies of energy transfer to the magnetosphere, *J.*
958 *Geophys. Res.*, **96**(A6), 9541–9548, doi: 10.1029/91JA00569.
- 959 Silverman, S. M. (1992), Secular variation of the aurora for the past 500 years, *Rev. Geophys.*, **30**
960 (4), 333–351, doi:10.1029/92RG01571.
- 961 Smith, E. J. and A. Balogh (1995) Ulysses observations of the radial magnetic field, *Geophys.*
962 *Res. Lett.*, **22**, 3317–3320, doi: 10.1029/95gl02826
- 963 Solanki, S. K., M. Schüssler, and M. Fligge (2000) Evolution of the Sun's large-scale magnetic
964 field since the Maunder Minimum, *Nature*, **408**, 445–447, doi:10.1038/35044027.
- 965 Solanki, S.K., M. Schüssler, and M. Fligge (2002) Secular variation of the Sun's magnetic flux,
966 *Astron. & Astrophys.*, **383**, 706–712, doi: 10.1051/0004-6361:20011790
- 967 Stamper, R., M. Lockwood, M.N. Wild, and T.D.G. Clark (1999) Solar Causes of the Long
968 Term Increase in Geomagnetic Activity, *J. Geophys Res.*, **104**, 28325–28342, doi:
969 10.1029/1999JA900311
- 970 Steinhilber, F., J. A. Abreu, J. Beer, and K. G. McCracken (2010) Interplanetary magnetic field
971 during the past 9300 years inferred from cosmogenic radionuclides, *J. Geophys. Res.*,
972 **115**, A01104, doi: 10.1029/2009JA014193
- 973 Svalgaard L., and E.W. Cliver (2010) Heliospheric magnetic field 1835–2009. *J. Geophys. Res.*,
974 **115** A09111, doi:10.1029/2009JA015069.
- 975 Svalgaard, L. and E.W. Cliver (2005) The IDV index: Its derivation and use in inferring
976 longterm variations of the interplanetary magnetic field strength, *J. Geophys. Res.*, **110**,
977 A12103, 2005, doi: 10.1029/2005JA011203
- 978 Temerin, M., and X. Li (2006) Dst model for 1995–2002, *J. Geophys. Res.*, **111**, A04221, doi:
979 10.1029/2005JA011257.
- 980 Tsurutani, B.T., W.D. Gonzalez, A.L.C. Gonzalez, F.L. Guarnieri, N. Gopalswamy, M. Grande,
981 Y. Kamide, Y. Kasahara, G. Lu, I. Mann, R. McPherron, F. Soraas, and V. Vasyliunas
982 (2006), Corotating solar wind streams and recurrent geomagnetic activity: A review, *J.*
983 *Geophys. Res.*, **111**, A07S01, doi:10.1029/2005JA011273.
- 984 Turner, N. E., W. D. Cramer, S. K. Earles, and B. A. Emery (2009), Geoefficiency and energy
985 partitioning in CIR-driven and CME-driven storms, *J. Atmos. Sol. Terr. Phys.*, **71**, 1023–
986 1031, doi:10.1016/j.jastp.2009.02.005
- 987 Usoskin, I. G., K. Mursula, S. K. Solanki, M. Schussler, and G. A. Kovaltsov (2002) A physical
988 reconstruction of cosmic ray intensity since 1610, *J. Geophys. Res.*, **107** (A11), 1374,
989 doi:10.1029/2002JA009343

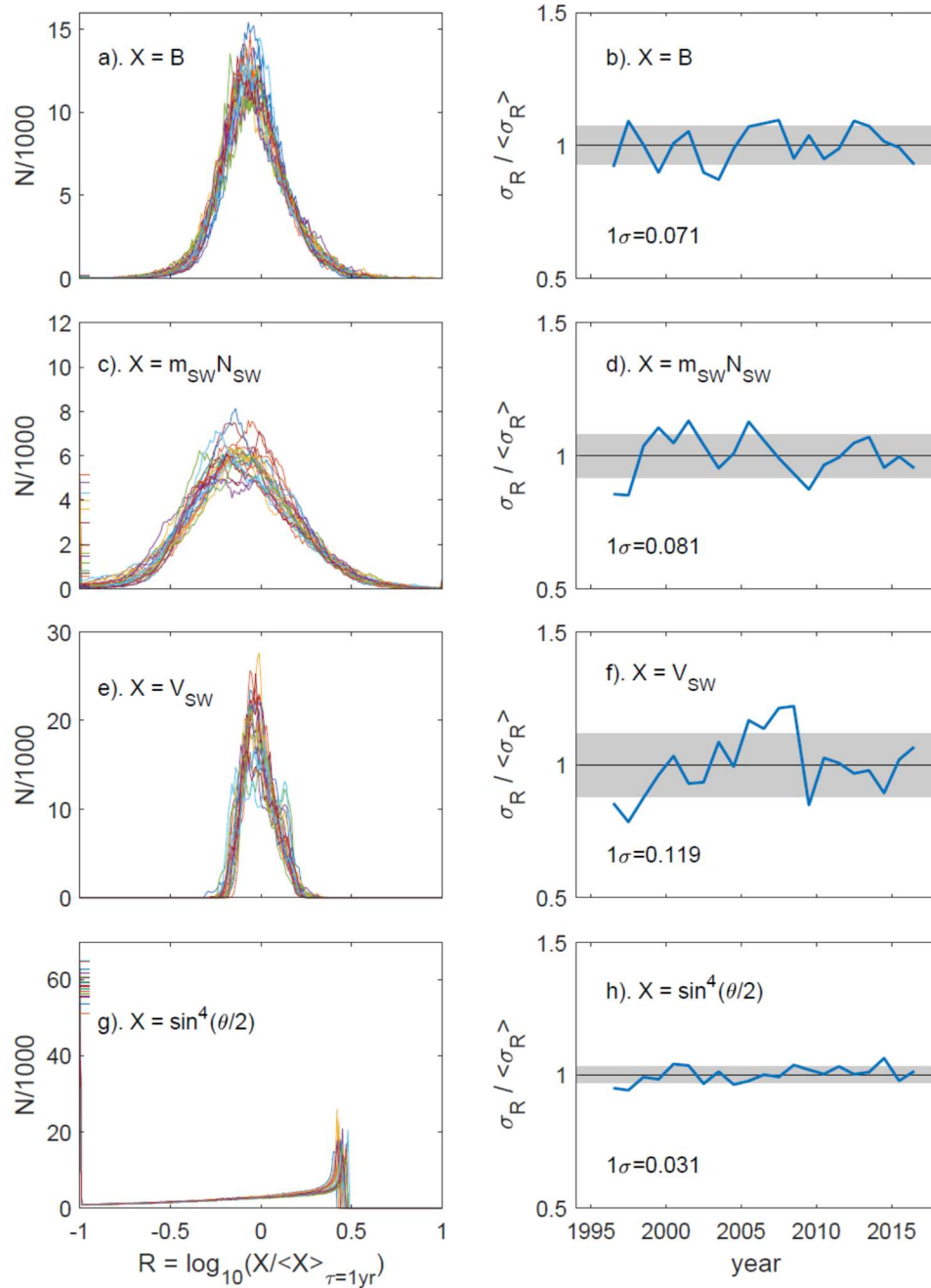
- 990 Vasyliunas, V. M., J. R. Kan, G. L. Siscoe, and S.-I. Akasofu (1982) Scaling relations governing
991 magnetospheric energy transfer, *Planet. Space Sci.*, **30**, 359–365, doi:
992 10.1016/00320633(82)90041-1
- 993 Vieira, L.E.A., and S.K. Solanki, Evolution of the solar magnetic flux on time scales of years to
994 millennia, *Astron. Astrophys.*, 509, A100, 2010, doi: 10.1051/0004-6361/200913276.
- 995 Vörös, Z., M. Leitner, Y. Narita, G. Consolini, P. Kovács, A. Tóth, and J. Lichtenberger (2015)
996 Probability density functions for the variable solar wind near the solar cycle minimum, *J.*
997 *Geophys. Res. Space Physics*, **120**, 6152–6166, doi: 10.1002/2015JA021257.
- 998 Wallis, D. D., and E. E. Budzinski (1981), Empirical models of height integrated conductivities,
999 *J. Geophys. Res.*, **86** (A1), 125–137, doi:10.1029/JA086iA01p00125.
- 1000 Wang Y.-M. and N. R. Sheeley, Jr. (2013) The solar wind and interplanetary field during very
1001 low amplitude sunspot cycles *Astrophys. J.*, **764**, 90, doi:10.1088/0004-637X/764/1/90
- 1002 Wang, Y.-M. and N.R. Sheeley Jr. (2002) Sunspot activity and the long-term variation of the
1003 Sun's open magnetic flux, *J. Geophys. Res.*, **107**, 1302, doi: 10.1029/2001JA000500
- 1004 Wang, Y.-M., J. Lean, and N.R Sheeley Jr. (2002) Role of a variable meridional flow in the
1005 secular evolution of the sun's polar fields and open flux, *Astrophys. J.*, **577**, L53–L57,
1006 doi: 10.1086/344196
- 1007 Wang, Y.-M., J. Lean, and N.R Sheeley Jr. (2005) Modeling the Sun's Magnetic Field and
1008 Irradiance since 1713, *Astrophys. J.*, **625** (1), 522–538, doi: 10.1086/429689

- 1009 Wang, Y.-M., S.H. Hawley, and N. R. Sheeley, Jr (1996) The magnetic nature of coronal holes,
1010 *Science*, **271**, 464–469, doi: 10.1126/science.271.5248.464
- 1011 Wygant, J. R., R. B. Torbert, and F. S. Mozer (1983) Comparison of S3-3 polar cap potential
1012 drops with the interplanetary magnetic field and models of magnetopause reconnection, *J.*
1013 *Geophys. Res.*, **88** (A7), 5727–5735, doi: 10.1029/JA088iA07p05727.

1014 **Figures**
 1015



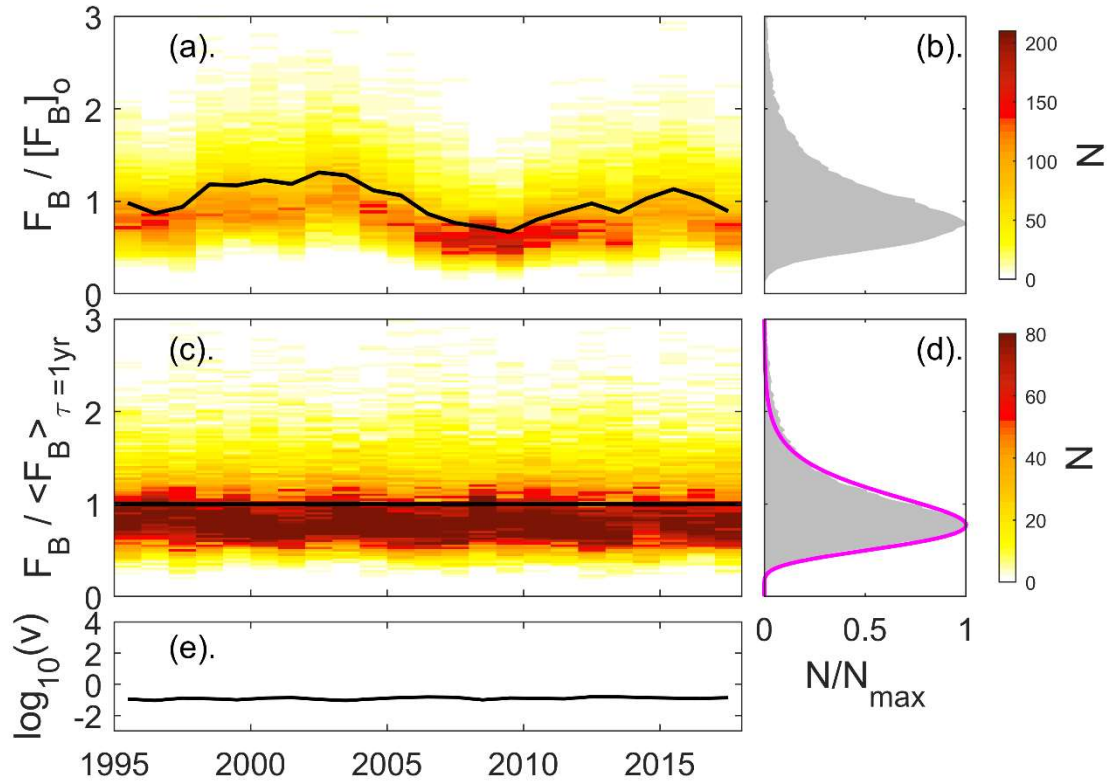
1016 **Figure 1.** Scatter plots of $f_{[X>X_0]}$, the fraction of days in a given year for which the daily mean
 1017 of a parameter X exceeds its 95 percentile X_0 computed over the whole dataset, as a function of
 1018 the annual mean of that parameter $\langle X \rangle_{\tau=1\text{yr}}$. In each panel, the mauve line is a third-order
 1019 polynomial fit to the data points, constrained to pass through the origin. (a) For the Ap index (Ap
 1020 being daily means of ap , data available for 1932-2016), for which the 95 percentile is $Apo = 38$;
 1021 (b) for the Dst index (data for 1957-2016), for which the 5-percentile $Dsto = -53\text{nT}$ (note in this
 1022 case, because Dst is increasingly negative as activity increases, $Dsto$ is the 5-percentile and
 1023 $f_{[Dst<Dst_0]}$ is shown); (c) for the AE index (data for 1967-2016), for which the 95 percentile is AE_0
 1024 $= 650\text{nT}$; (d) for the AU index (data for 1967-2016), for which the 95 percentile is $AU_0 = 228\text{nT}$;
 1025 (e) for the AL index (data for 1967-2016), for which the 5-percentile $AL_0 = -444\text{nT}$ (note in this
 1026 case, because AL is increasingly negative as activity increases, AL_0 is the 5-percentile and
 1027 $f_{[AL<AL_0]}$ is shown); and (e) the power input into the magnetosphere for a coupling exponent of α
 1028 $= 0.44$, P_α (data for 1963-2016, although some years are omitted as data availability is too low –
 1029 see Paper 1), for which the 95-percentile is $P_{\alpha 0} = 2.73 P_0$, where P_0 is the mean P_α for all
 1030 available data. In Paper 1 we derive an optimum value for P_0 of 0.38×10^{19} W (although note that,
 1031 unlike P_α / P_0 , this value is very sensitive on the derived coupling function, α) which yields an
 1032 absolute estimate of the 95-percentile for the power input into the magnetosphere of $P_{\alpha 0} =$
 1033 1.04×10^{19} W.



1034
1035
1036
1037
1038

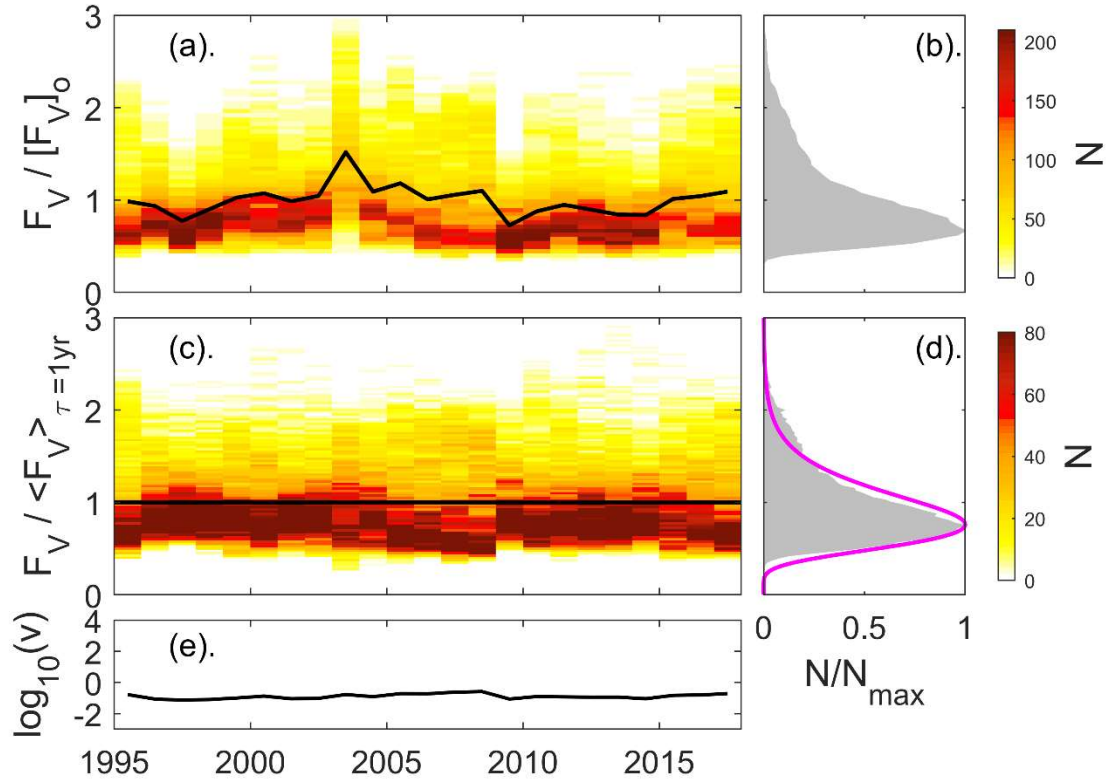
Figure 2. Analysis of annual distributions of the 11046240 1-minute averages of parameters contributing to the power input into the magnetosphere, P_a for 1996-2017 (inclusive). The left hand plots show 22 superposed annual distributions for individual years of $R = \log_{10}(X / \langle X \rangle_{\tau=1\text{yr}})$ where X is (a) the IMF, B ; (c) the solar wind

1039 mass density, $m_{\text{sw}}N_{\text{sw}}$; (e) the solar wind speed, V_{sw} ; and (g) the IMF orientation
 1040 factor $\sin^4(\theta_{\text{GSM}}/2)$. $\langle X \rangle_{\tau=1\text{yr}}$ is the corresponding annual mean value in each case.
 1041 Lognormal distributions in $X/\langle X \rangle_{\tau=1\text{yr}}$ would give Gaussian distributions in R ,
 1042 centered on zero. The vertical axis is $N/1000$, where N the number of 1-minute
 1043 averaged samples in bins of R that are 0.01 wide. Note that in these left-hand plots
 1044 the extreme bins are for $R \leq -0.99$ and $R \geq +0.99$ and the numbers of samples in
 1045 these extreme bins are given for individual years by colored tick marks on the left
 1046 and right (respectively) vertical axes of (a), (c), (e) and (g). There are negligibly few
 1047 samples in the $R \geq 0.99$ bin for all four cases (7 for B , 1770 for $m_{\text{sw}}N_{\text{sw}}$, and none for
 1048 either $\sin^4(\theta_{\text{GSM}}/2)$ or V_{sw}). The same is not always true for the $R \leq -0.99$ bin (for
 1049 which, in total, there are 1597 samples for B , 36818 for $m_{\text{sw}}N_{\text{sw}}$ (0.3% of the total),
 1050 2351900 (21% of the total) for $\sin^4(\theta_{\text{GSM}}/2)$ and none for V_{sw}). In particular, the peak
 1051 N in part (g) is always for this $R \leq -0.99$ bin and varies between 57530 and 68225,
 1052 depending the year. Note that in many cases these coloured tick marks are
 1053 indistinguishable from the x axis (at $N = 0$). The corresponding right hand plots (b),
 1054 (d), (f) and (h) show the variations in the standard deviations of the distributions, σ_R
 1055 for each year (normalized to their overall means for all years, i.e. $\sigma_R/\langle \sigma_R \rangle$). The
 1056 horizontal black line in each plot gives the mean value (by definition unity), and the
 1057 surrounding grey areas show plus and minus one standard deviation about this mean.
 1058

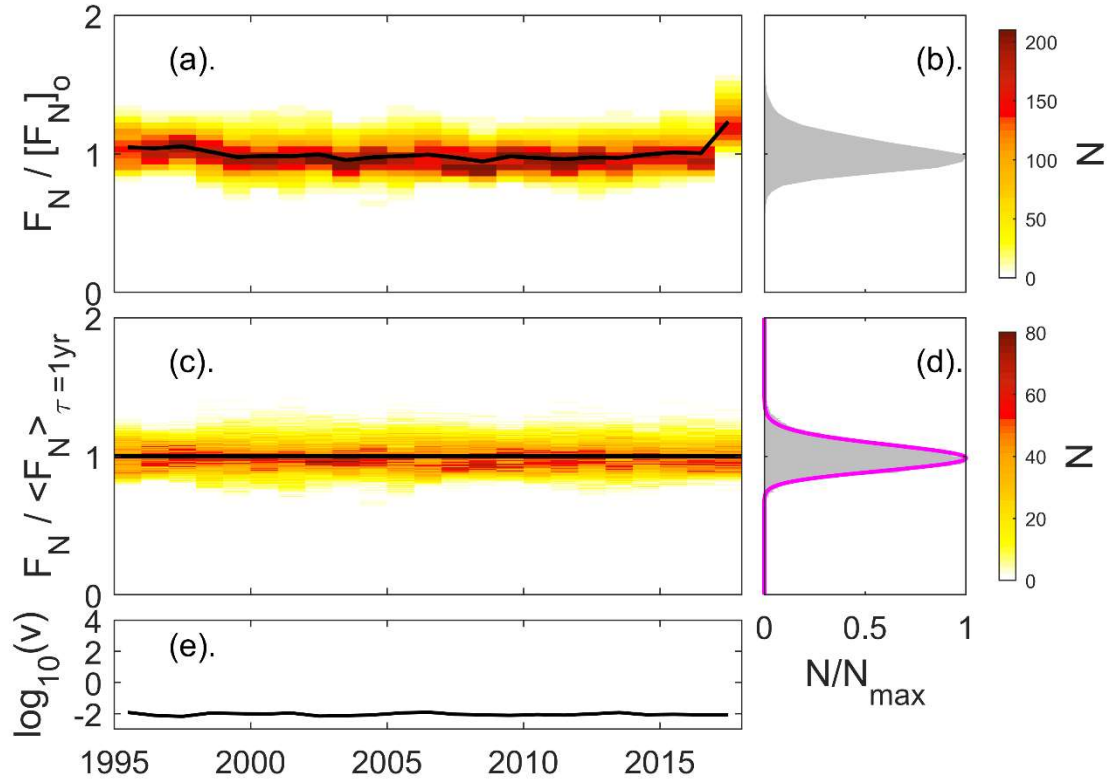


1059

1060 **Figure 3.** Analysis of the F_B term in P_α . (a) The annual distributions of 3-hourly values of
 1061 $F_B/[F_B]_o$ (where $[F_B]_o$ is the mean of F_B for all the data from 1995-2017): the number of samples
 1062 N in bins of $F_B/[F_B]_o$ that are 0.01 wide is color-contoured as function of year. The black line
 1063 shows the annual mean values, plotted in the middle of the year. (b) The normalized distribution
 1064 of $F_B/[F_B]_o$ for all years is shown as a grey histogram of N/N_{max} , where N_{max} is the peak value of
 1065 N . (c) The annual probability density of 3-hourly values of $F_B/\langle F_B \rangle_{\tau=1yr}$ (where $\langle F_B \rangle_{\tau=1yr}$ is the
 1066 annual mean of F_B for the year in question), color-contoured as function of year. The blackline
 1067 shows the annual mean values which, by definition, are unity. (d) The normalized distribution of
 1068 $F_B/\langle F_B \rangle_{\tau=1yr}$ for all years is shown by the grey histogram which has been fitted with log-normal
 1069 form with a mean of unity and a variance $\nu = 0.120$ (mauve line). (e) The logarithm of variance,
 1070 ν of the distributions.



826 **Figure 4.** Analysis of the F_V term in P_α in the same format as figure 3. The normalized distribution of $F_V / \langle F_V \rangle_{\tau=1\text{yr}}$ for $\tau = 3\text{hrs}$ and all years is shown in (d) by the grey histogram which has been fitted with log-normal distribution with a mean of unity and a variance $\nu = 0.127$ (mauve line).



829

830

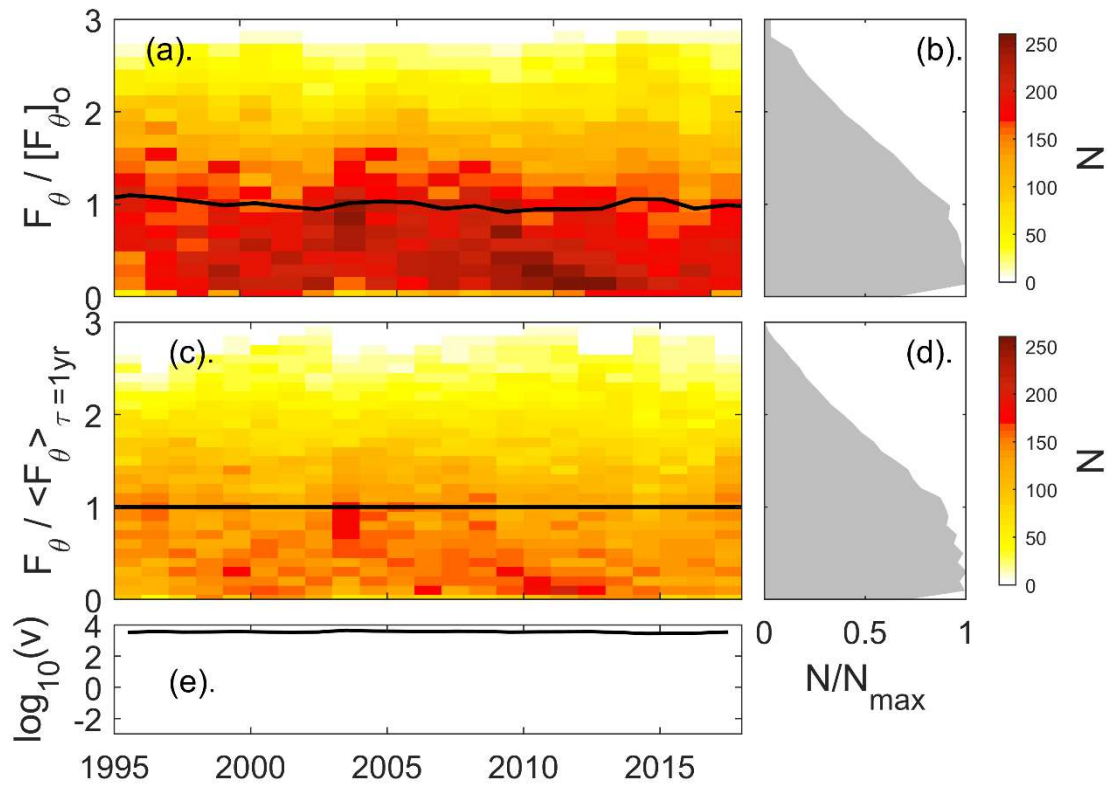
831

832

833

Figure 5. Analysis of the F_N term in P_α in the same format as figure 3. The normalized distribution of $F_N / \langle F_N \rangle_{\tau=1\text{yr}}$ for $\tau = 3\text{hrs}$ and all years is shown in (d) by the grey histogram which has been fitted with log-normal distribution with a mean of unity and a variance $\nu = 0.009$ (mauve line).

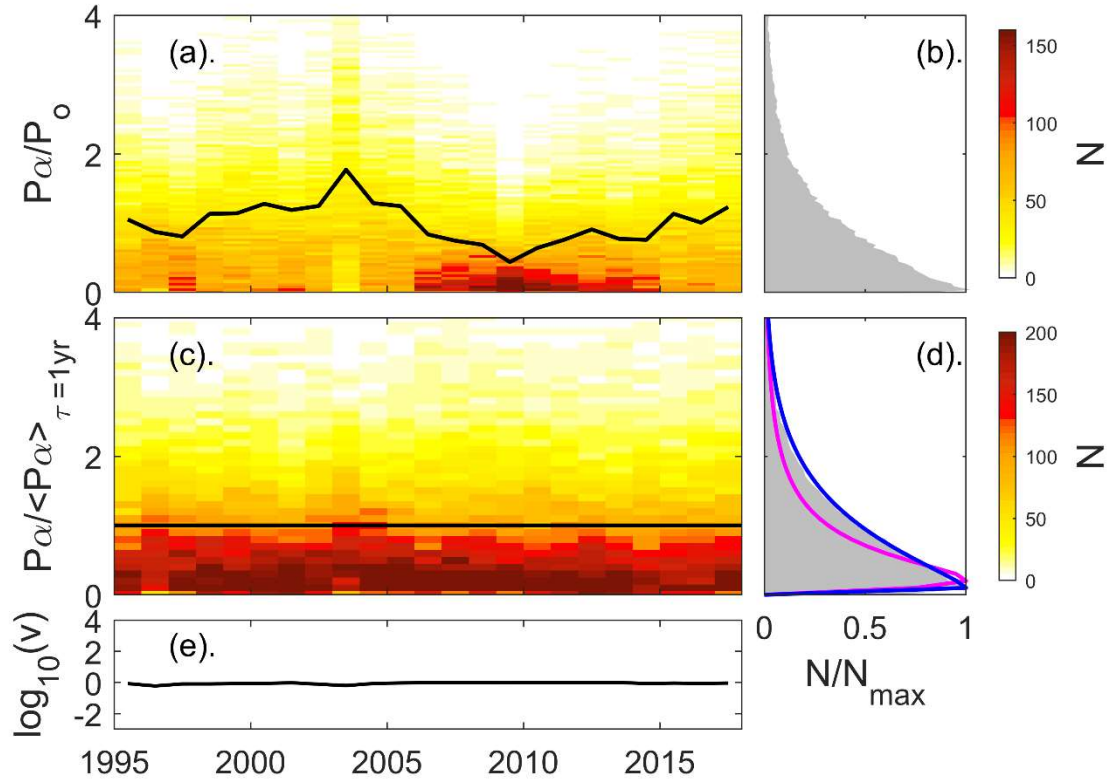
834



835

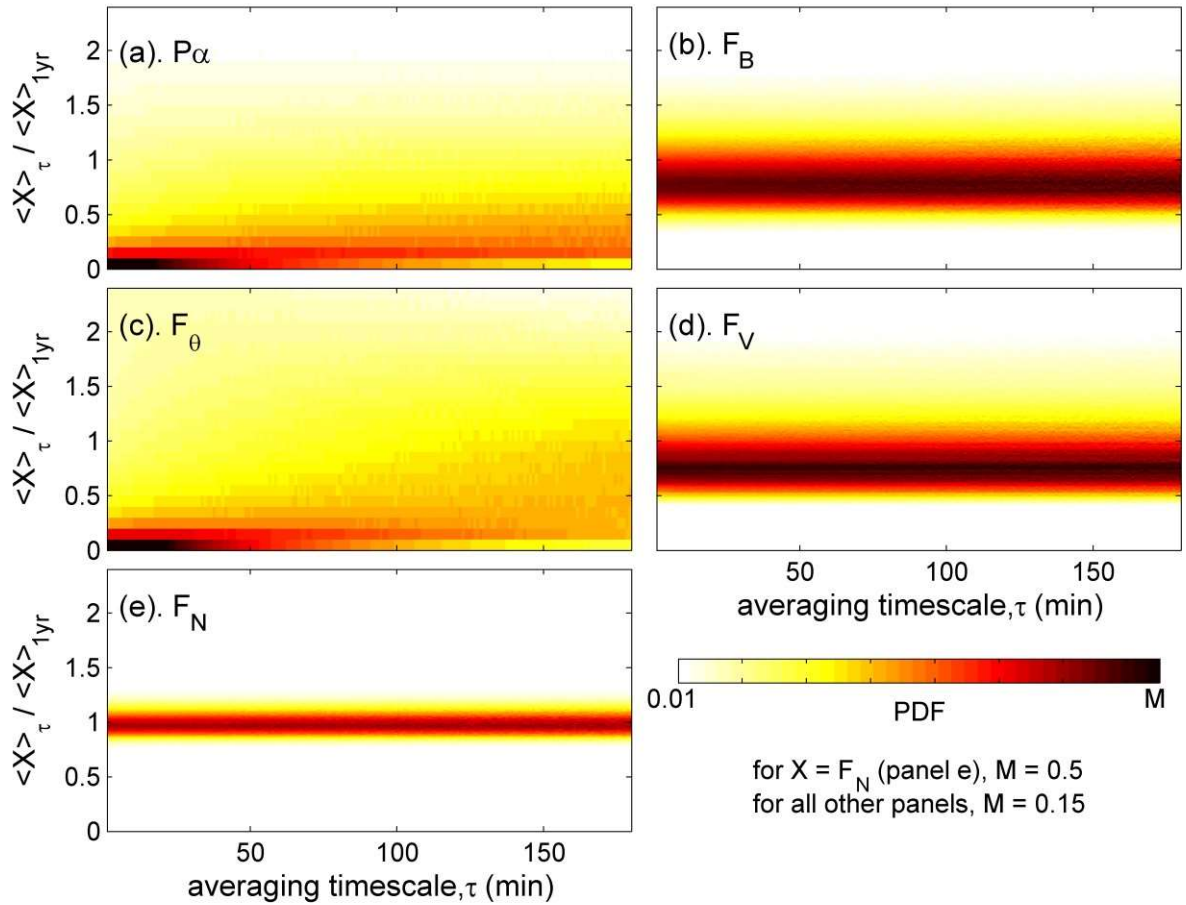
836 **Figure 6.** Analysis of the F_θ term in P_α in the same format as figure 3. The normalized
 837 distribution of $F_\theta / \langle F_\theta \rangle_{\tau=1\text{yr}}$ for $\tau = 3\text{hrs}$ and all years is shown in (d) by the grey histogram
 838 which has not been fitted with a distribution as it does not match well any standard form. The
 839 mean of the annual variance values is $\langle v \rangle = 3.542 \times 10^3$.

840



841

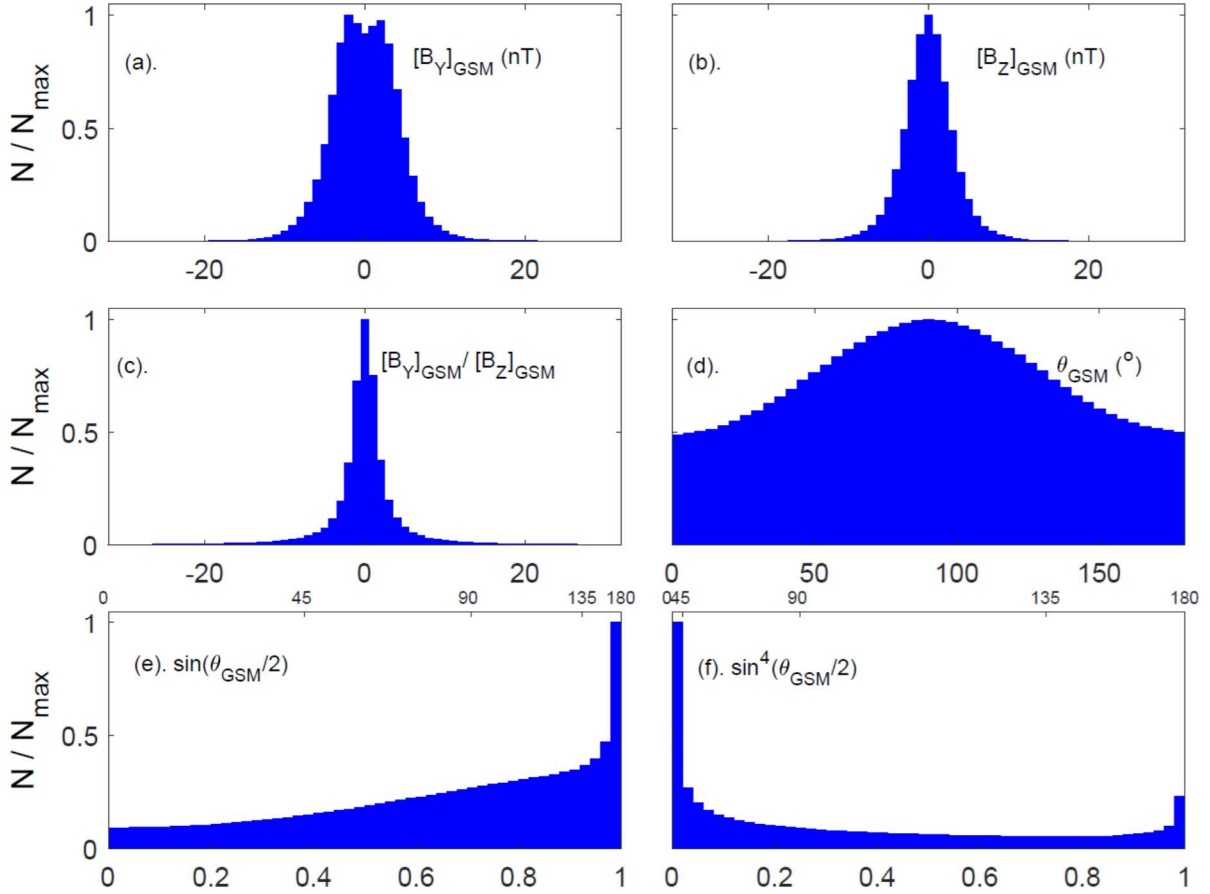
842 **Figure 7.** Analysis of P_α in the same format as figure 3. The normalized distribution of
 843 $P_\alpha / \langle P_\alpha \rangle_{\tau=1\text{yr}}$ for $\tau = 3\text{hrs}$ and all years is shown in (d) by the grey histogram which has been
 844 fitted with log-normal distribution with a mean of unity and a variance $v = 1.788$ ($\mu = -0.5127$,
 845 mauve line) and a Weibull distribution with $k = 1.0625$ and $\lambda = 1.0240$ (blue line).



846

847

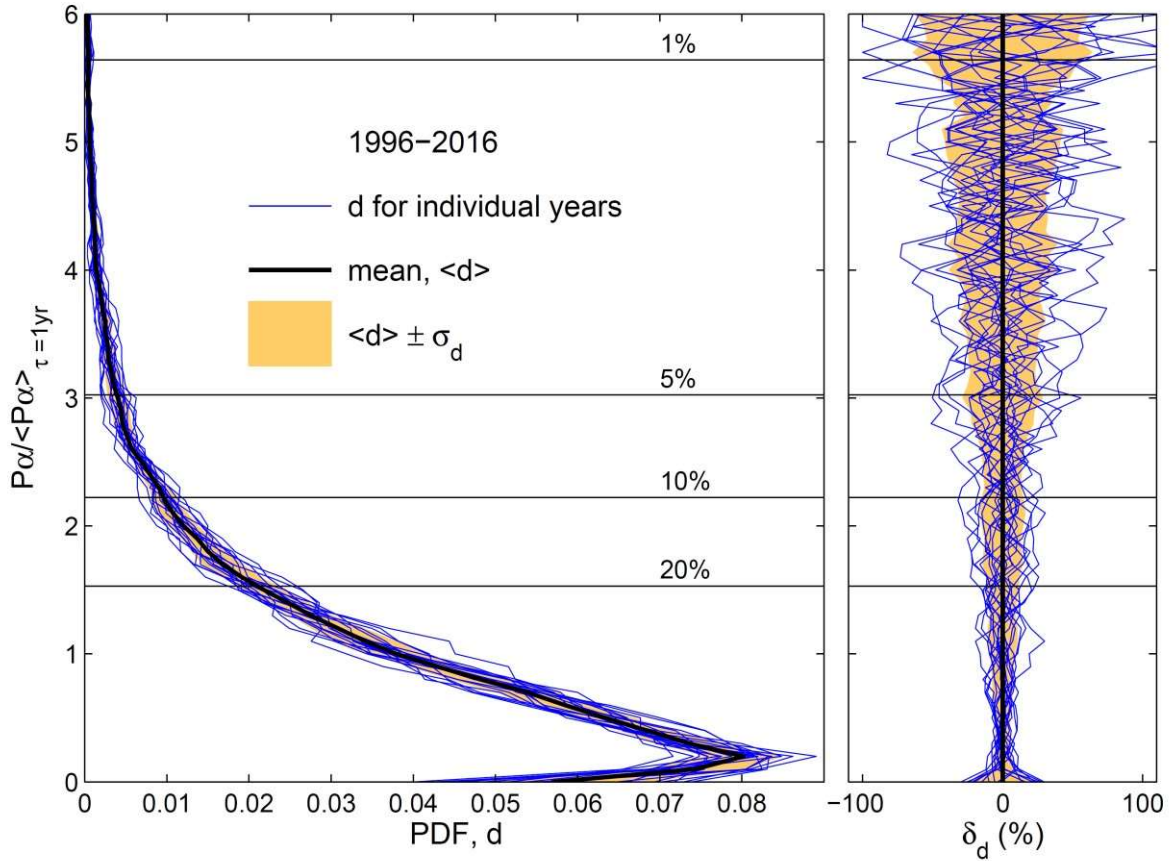
848 **Figure 8.** Analysis of the origin of the Weibull distribution of $\langle P_\alpha \rangle_\tau / \langle P_\alpha \rangle_{\tau=1\text{yr}}$ for $\tau = 3\text{hrs}$ and
 849 all years, as shown in Figure 7d. In each panel, the PDF for a given τ is given as a vertical slice
 850 and τ varies along the horizontal axis between 1 min. and 3 hours. The panels are for: (a)
 851 $\langle P_\alpha \rangle_\tau / \langle P_\alpha \rangle_{\tau=1\text{yr}}$; (b) $\langle F_B \rangle_\tau / \langle F_B \rangle_{\tau=1\text{yr}}$; (c) $\langle F_\theta \rangle_\tau / \langle F_\theta \rangle_{\tau=1\text{yr}}$; (d) $\langle F_V \rangle_\tau / \langle F_V \rangle_{\tau=1\text{yr}}$; and (e)
 852 $\langle F_N \rangle_\tau / \langle F_N \rangle_{\tau=1\text{yr}}$.



853

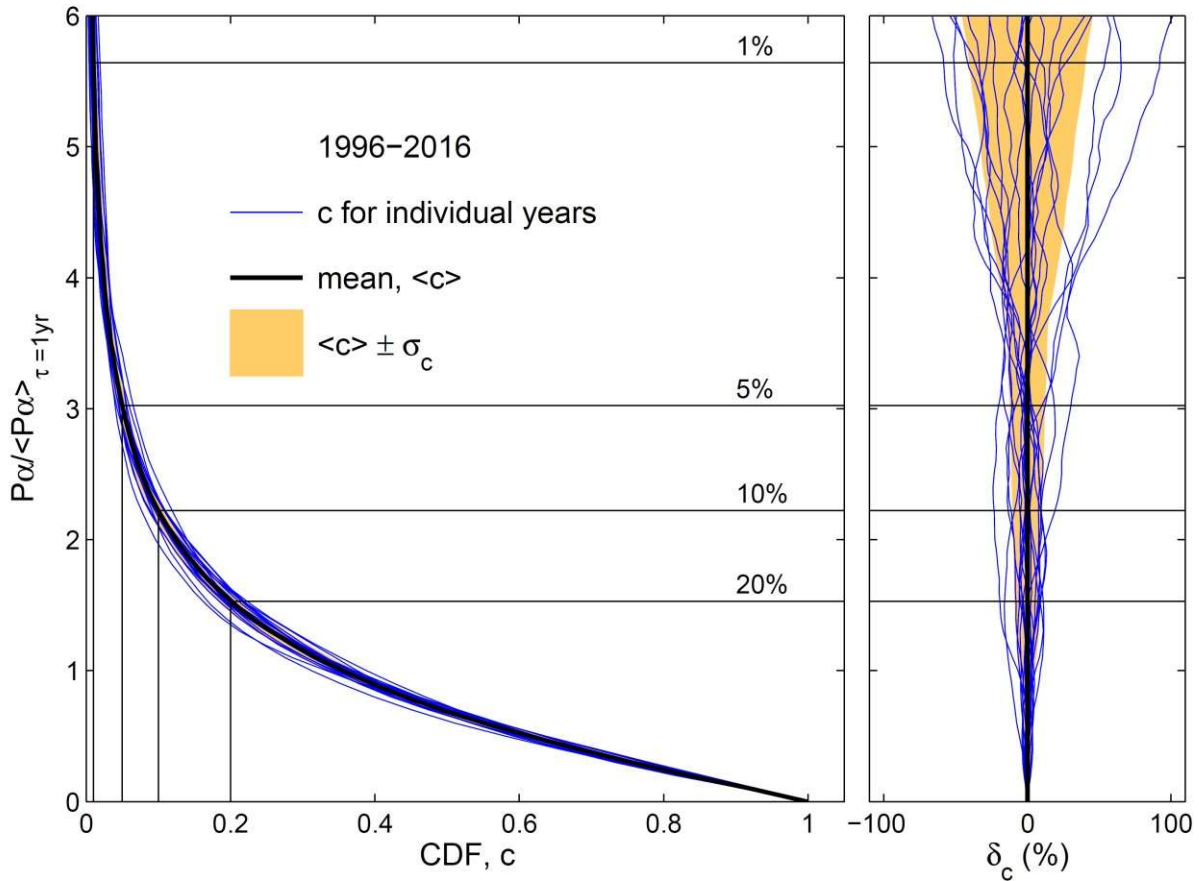
854 **Figure 9.** Analysis of the 10207789 valid 1-minute averages of the $\sin^4(\theta_{\text{GSM}}/2)$ term obtained
 855 in the years 1996-2016 (inclusive). The distribution of: (a) the IMF B_Y component in the GSM
 856 frame, $[B_Y]_{\text{GSM}}$; (b) the IMF B_Z component in the GSM frame, $[B_Z]_{\text{GSM}}$; (c) the ratio,
 857 $[B_Y]_{\text{GSM}}/[B_Z]_{\text{GSM}}$; (d) the IMF clock angle in the GSM frame, $\theta_{\text{GSM}} = \arctan(|[B_Y]_{\text{GSM}}|/[B_Z]_{\text{GSM}})$
 858 ; (e) $\sin(\theta_{\text{GSM}}/2)$; and (f) $\sin^4(\theta_{\text{GSM}}/2)$. In each panel N is the number of samples per bin and N_{max}
 859 is the maximum value of N . In panels (e) and (f) the non-linear scales along the top (in small
 860 font) give the clock angle θ_{GSM} (in degrees) which corresponds to the lower scale, which is
 861 $\sin(\theta_{\text{GSM}}/2)$ in (e) and in $\sin^4(\theta_{\text{GSM}}/2)$ in (f).

862



863

864 **Figure 10.** (a) Probability distribution function PDF, d , of $\langle P_\alpha \rangle_\tau / \langle P_\alpha \rangle_{\tau=1\text{yr}}$ for $\tau = 3\text{hrs}$. The
 865 black line is the overall distribution for all 21 years (as shown in figure 7d) and the blue lines are
 866 the values for individual years. The orange area is the mean of the annual values, plus and minus
 867 one standard deviation. Horizontal black lines are shown for the cumulative probability levels of
 868 1%, 5%, 10% and 20%. (b). The percentage deviations of d from the mean, $\delta_d = 100(d - \langle d \rangle) / \langle d \rangle$
 869 in the same format.



870

871 **Figure 11.** (a) Cumulative distribution functions CDF, c , of $\langle P_\alpha \rangle_{\tau=1\text{yr}}$ for $\tau = 3\text{hrs}$,
 872 corresponding to the PDFs in figure 10. The black line is the overall distribution for all 21 years
 873 and the blue lines are the values for individual years. The orange area is the mean of the annual
 874 values, plus and minus one standard deviation. Horizontal black lines are shown for the
 875 cumulative probability levels of 1%, 5%, 10% and 20%. (b). The percentage deviations of c
 876 from the mean, $\delta_c = 100(c - \langle c \rangle) / \langle c \rangle$ in the same format.